

Journal Pre-proof

Mineralization proximal to the final Nuna suture in northeastern Australia

Hugo K.H. Olierook, Robert G. Affleck, Noreen J. Evans, Fred Jourdan, Christopher L. Kirkland, Silvia Volante, Adam R. Nordsvan, Brent I. McInnes, Bradley McDonald, Celia Mayers, R. Adam Frew, Kai Rankenburg, Nic d'Offay, Max Nind, Adrian Larking



PII: S1342-937X(20)30329-4

DOI: <https://doi.org/10.1016/j.gr.2020.12.017>

Reference: GR 2478

To appear in: *Gondwana Research*

Received date: 24 April 2020

Revised date: 22 November 2020

Accepted date: 19 December 2020

Please cite this article as: H.K.H. Olierook, R.G. Affleck, N.J. Evans, et al., Mineralization proximal to the final Nuna suture in northeastern Australia, *Gondwana Research* (2020), <https://doi.org/10.1016/j.gr.2020.12.017>

This is a PDF file of an article that has undergone enhancements after acceptance, such as the addition of a cover page and metadata, and formatting for readability, but it is not yet the definitive version of record. This version will undergo additional copyediting, typesetting and review before it is published in its final form, but we are providing this version to give early visibility of the article. Please note that, during the production process, errors may be discovered which could affect the content, and all legal disclaimers that apply to the journal pertain.

© 2020 Published by Elsevier.

Mineralization proximal to the final Nuna suture in northeastern Australia

Hugo K. H. Olierook^{1,2,*}, hugo.olierook@curtin.edu.au, Robert G. Affleck³, Noreen J. Evans^{1,2}, Fred Jourdan^{1,2,4}, Christopher L. Kirkland^{1,1}, Silvia Volante^{1,5,6}, Adam R. Nordsvan^{1,5,7}, Brent I. McInnes², Bradley McDonald^{1,2}, Celia Mayers^{1,2,4}, R. Adam Frew^{1,2,4}, Kai Rankenburg¹, Nic d'Offay³, Max Nind³, Adrian Larking³

¹School of Earth and Planetary Sciences, Curtin University, GPO Box U1987, Perth, WA 6845, Australia

²John de Laeter Centre, Curtin University, GPO Box U1987, Perth, WA 6845, Australia

³Moho Resources Ltd., 1/46 Salvado Rd, Wembley, Perth, WA 6014, Australia

⁴Western Australian Argon Isotope Facility, Curtin University, Perth, WA 6845, Australia

⁵Earth Dynamics Group, Australian Research Council Centre of Excellence for Core to Crust Fluid Systems (CCFS) and The Institute for Geoscience Research (TIGeR), Curtin University, GPO Box U1987, Perth, WA 6845, Australia

⁶Institute of Geology, Mineralogy and Geophysics, Ruhr-Universität Bochum, Universitätsstraße 150, 44801, Bochum, Germany

⁷Department of Earth Sciences, University of Hong Kong, Pokfulam, Hong Kong

*Corresponding author.

Handling Editor: J.G. Meert

Abstract

Mineralization along continental suture zones is facilitated through the frequent presence of pathways from fertile mantle source regions to crustal repositories. Due to their inherent rheological weakness, these suture zones are often concealed, which hinders surface-based observations. Here, we use zircon U-Pb and sericite $^{40}\text{Ar}/^{39}\text{Ar}$ dating, and whole-rock geochemical data to investigate the crystallization and mineralization history from a sequence of granites (*sensu lato*), volcanic rocks and sedimentary rocks from the Au–Ag–Pb–Zn Empress Springs Project in northeast Australia, which are under >50 m of Phanerozoic cover and located near the interpreted ca. 1.6 Ga tectonic boundary between the North Australia Craton (Mount Isa Inlier) and Laurentia (Georgetown Inlier). Zircon U-Pb dating indicates that granite emplacement, volcanic eruptions and dolerite intrusions occurred between 1564 ± 6 and 1546 ± 13 Ma (2σ), corresponding to the 1560–1550 Ma Esmeralda Supersuite and the Croydon Volcanic Group exposed in the western Georgetown Inlier. U-Pb ages from detrital zircon grains in a sedimentary rock revealed a near unimodal ca. 1560 Ma population, likely sourced from the surrounding granitic and volcanic rocks. Sericite $^{40}\text{Ar}/^{39}\text{Ar}$ dating yielded disturbed spectra with evidence for incorporation of excess radiogenic Ar, but with a probable Carboniferous to Permian age, potentially dating the timing of gold mineralization. Geochemical similarities point towards an epithermal origin for the Empress Springs Project, consistent with post-orogenic mineralization at either ca. 1560–1550 Ma or 330–250 Ma. It is likely that a series of west-dipping lithospheric-scale faults below the Empress Springs Project, here termed the Empress Suture Zone, demarcate the final suture zone associated with the assembly of Nuna. Reactivation of the Empress Suture Zone ~1.3 b.y. after crystallization with potential contemporaneous gold mineralization attests to its longevity for fluid mobility.

Keywords: Empress Springs; Columbia; Laurentia; North Australian Craton; zircon U-Pb; epithermal

1 INTRODUCTION

Suture zones are major terrane bounding structures that form in accretionary and collisional orogens. Due to their inherent structural weakness, suture zones provide direct pathways from metallogenic mantle source regions to crustal mineralization sinks (Groves and Bierlein, 2007). Mineralization along suture zones can: (i) predate continent amalgamation, with mineralization now incorporated in the suture zone (e.g., volcanic-hosted massive sulfide; Barrote et al., 2010; Deng et al., 2016), (ii) be contemporaneous with continent–continent collision or terrane accretion (e.g., orogenic gold or porphyry copper; Cawood and Hawkesworth, 2015; Groves et al., 1998; Hou et al., 2015), or (iii) postdate terrane assembly, exploiting major transcrustal fluid flow corridors (e.g., iron oxide copper-gold, hydrothermal gold or porphyry Mo; Bao et al., 2017; Groves et al., 2010; Heinhorst et al., 2000; Olierook et al., 2018; Sarma et al., 2011). Therefore, suture zones are commonly targeted for mineral exploration because of the ability to record multiple mineralizing and upgrading events through structural corridors (Li et al., 2017; Pirajiro and Bagas, 2002; Zheng et al., 2014; Zi et al., 2015). However, structural weaknesses associated with suture zones can also be problematic for exploration since many are buried under cover due to the ease of weathering and erosion of hydrothermally-altered lithologies (Johnson et al., 2013; Olierook et al., In Press; Spaggiari et al., 2018; Tohver et al., 2005). Thus, the precise location and mineralizing potential of many suture zones remain poorly understood.

One example that has recently come into focus is the position of the final suture zone associated with the assembly of the supercontinent Nuna (also known as Columbia; e.g., Meert, 2002; Meert, 2012; Meert and Santosh, 2017) in northeastern Australia (Nordsvan et al., 2018; Pourceau et al., 2018). Various workers have attributed the collision between the North Australian Craton (\pm South Australian Craton) and Laurentia at ca. 1600 Ma as the final convergent event before the breakup of the supercontinent (Betts et al., 2016; Furlanetto et al., 2016; Kirscher et al., 2019; Pehrsson et al., 2016;

Pisarevsky et al., 2014). In northeastern Australia, seismic and geochronological data have been used to suggest that this suture zone is buried under Phanerozoic cover between the Mount Isa and Georgetown Inliers, which were originally part of the North Australian and Laurentian cratons, respectively, prior to the assembly of Nuna (Korsch et al., 2012). However, the position of the suture zone (or zones) remains debated. Korsch et al. (2012) and Betts et al. (2016) considered the Gidyea Suture Zone, located east of the Mount Isa Inlier, to mark the boundary between rocks of North Australian and Laurentian affinity (Fig. 1c, d). Conversely, Pourteau et al. (2018) posited that the terrane boundary was situated directly west of the outcropping Georgetown Inlier, interpreting a lithospheric-scale unnamed fault within the Numil Seismic Province as equating to the suture zone (Fig. 1c,d). The precise position of the suture zone between the North Australian Craton and Laurentia remains unknown due to the paucity of work in the covered region between the Mount Isa and Georgetown Inliers. Constraining which model, if either, is correct would aid tectonic reconstructions and elucidate the nature and likely positions of mineralization.

A drilling program was recently completed by Moho Resources Ltd across the Empress Springs Au-Ag-Zn-Pb project (Moho Resources, 2019d), located ~20 km southwest of the outcropping Georgetown Inlier where a series of west-dipping lithospheric-scale faults are interpreted to intersect the surface (Fig. 1; Korsch et al., 2012; Pourteau et al., 2018). These drill holes intersected granites, intermediate to felsic volcanic rocks, mafic intrusions and sedimentary rocks below ~50 m of Phanerozoic cover (Fig. 2; Moho Resources, 2019d). Geochemical analyses of selected samples revealed a virgin discovery of up to 2.3 ppm of Au, 2.5 ppm Ag, 0.26% Zn, and 0.14% Pb hosted in quartz-sericite altered granites (Fig. 2; Moho Resources, 2019d). Two major questions remain. (1) What is the crystallization age of the encountered rocks, and do they have a North Australian (Mount Isa) or Laurentian (Georgetown) affinity? (2) When did mineralization occur and did a Nuna construction-related suture play a significant role in mineralization?

Here, we present ten zircon U-Pb and two sericite $^{40}\text{Ar}/^{39}\text{Ar}$ isotopic data sets from the Empress Springs Project to help address both the crystallization and mineralization ages, respectively.

Ultimately, the geochronological data sets presented allow us to refine the position of the Nuna suture and help ascertain the longevity of this zone of lithospheric weakness.

2 GEOLOGICAL BACKGROUND

2.1 Geological history and setting of the Mount Isa Inlier

The Mount Isa Inlier preserves ~400 m.y. history of sedimentation and igneous activity from the late Paleo- to early Mesoproterozoic. The inlier has been divided into 15 fault bound domains in three broad N–S trending belts that account for geochronology, basin evolution, structural grain, and metamorphic grade (Day et al., 1983; Geological Survey of Queensland, 2011). The oldest rocks in the Mount Isa Inlier are metamorphosed sedimentary rocks that were deposited pre-1870 Ma, likely during broadly SW–NE directed extension (de Vries et al., 2008). At ca. 1870–1840 Ma, the Barramundi Orogeny resulted in E–W directed shortening, mostly recorded in the central belt of the Mount Isa Inlier (Etheridge et al., 1987; Page and Williams, 1988). Late stages of the Barramundi Orogeny are associated with emplacement of voluminous granites (*sensu lato*) and associated volcanic rocks (Withnall et al., 2013). The Barramundi Orogeny may have been associated with a collision between the North Australian Craton and Laurentia (Betts et al., 2016) or the North Australian Craton and the central belt of the Mount Isa Inlier (Bierlein et al., 2011). Even if the North Australian Craton and Laurentia collided at this time (Betts et al., 2016), a later reorganization occurred in order to accommodate younger paleomagnetic poles at ca. 1.65 Ga (Kirscher et al., 2019).

Following the Barramundi Orogeny, the Mount Isa Inlier underwent a complex rifting history characterized by sequential deposition of three superbasins that spanned ~200 m.y. (Betts et al., 2016; Gibson et al., 2018; Southgate et al., 2013). The oldest basin, the Leichhardt Superbasin (ca. 1790–1740 Ma), is mostly confined to the western belt (Holcombe et al., 1991; O'Dea et al., 1997a) and was probably associated with the Gawler Craton rifting from the North Australian Craton (Giles et al., 2002). An episode of E–W directed shortening followed deposition of the Leichardt Superbasin (Betts, 1999; O'Dea et al., 1997b), possibly related to accretion of the seismically-imaged Numil

province (Fig. 1c; Blaikie et al., 2017). Succeeding this event, renewed extension accommodated deposition of the Calvert Superbasin between ca. 1720 and 1690 Ma (Betts et al., 2011; Jackson et al., 2000). Sedimentation in the inlier was interrupted for ~30 m.y. between deposition of the Calvert Superbasin and the overlying Isa Superbasin (ca. 1660–1600 Ma), associated with the emplacement of fractionated I-type granites in the western belt (Gibson et al., 2008; Wyborn et al., 1998).

Sedimentation in the Mount Isa Inlier mostly ceased at the onset of the Isan Orogeny at ca. 1620 or 1600 Ma (Betts and Giles, 2006; Giles et al., 2002; O'Dea et al., 1997b). Deformational structures of the Isan Orogeny are associated with N–S directed crustal shortening during the early stage of the orogeny (Lister et al., 1999; O'Dea et al., 2006; O'Dea et al., 1997a; O'Dea et al., 1997b), followed by a major E–W to SE–NW directed shortening stage, developing dominant N-trending compressional structures (Blenkinsop et al., 2008; MacCready et al., 1997; O'Dea et al., 2006). The latest deformation phase of the Isan Orogeny was associated with the emplacement of a ca. 1550 Ma tonalite–trondhjemite–granodiorite suite derived from high-pressure partial melting of mafic, mantle-derived sources (Mark, 2001; Page and Sun, 1998; Volante et al., 2020a; Wyborn, 1998), and subsequent voluminous ca. 1540–1490 Ma A-type granites assigned to the Williams Supersuite (Page and Sun, 1998; Wyborn, 1998).

2.2 Geological history and setting of the Georgetown Inlier

The Georgetown Inlier is characterized by upper Paleo- to lower Mesoproterozoic sedimentary rocks. The lower Etheridge Group represents the oldest sedimentary rocks, deposited between ca. 1700 and 1650 Ma, and have a detrital zircon provenance that strongly resembles that of sedimentary rocks deposited at the same time in Laurentia (Furlanetto et al., 2016; Neumann and Kositcin, 2011; Nordsvan et al., 2018). The sedimentary sequence was interbedded with ca. 1665 Ma tholeiitic basalts (Baker et al., 2010), and intruded by dolerite dykes and sills at ca. 1655 Ma (Black et al., 1998). The upper sequence (i.e., upper Etheridge Group) is characterized by fine-grained sedimentary rocks that were not intruded by the dolerite dykes or sills (Black et al., 1998; Withnall et al., 1988). These

sedimentary rocks have a different zircon provenance from those of the lower sequence (Neumann and Kositcin, 2011; Nordsvan et al., 2018) and more juvenile ϵNd values (Lambeck et al., 2012).

Recent metamorphic studies divided the Georgetown Inlier into four main metamorphic domains: (i) very low-grade rocks in the westernmost Croydon Domain, (ii) greenschist-facies Western Domain, (iii) medium- to upper amphibolite-facies Central Domain, and (iv) upper amphibolite- to granulite-facies Eastern Domain (Volante et al., In Press). From ca. 1600–1550 Ma, the Etheridge Group was polydeformed and metamorphosed during the Jana Orogeny (Boger and Hansen, 2004; Cihan et al., 2006; Pourteau et al., 2018; Volante et al., 2020b; Volante et al., In Press; Withnall et al., 2013).

During the ca. 1560–1550 Ma post-collisional stage of the orogeny, the Georgetown Inlier was intruded by voluminous S-type and minor I-type granites and concomitant felsic to intermediate volcanic rocks, capping the sedimentary sequence to the west (Black and McCulloch, 1990; Neumann and Kositcin, 2011; Nordsvan et al., in review; Volante et al., 2020a; Withnall, 1996; Withnall et al., 2013). Generally, the Georgetown Inlier granites are categorized into three main petrological groups: the Forsayth Supersuite, Forest Home Supersuite, and Esmeralda Supersuite (Champion, 1991; Withnall et al., 2013). The Forsayth Supersuite is situated in the Central Domain of the Georgetown Inlier (Budd et al., 2001; Champion, 1991; Volante et al., In Press; Withnall et al., 2013) and derives from the melting of the surrounding high-grade metasedimentary host-rocks (Black and McCulloch, 1990). The Forest Home Supersuite consists of the Forest Home and Talbot Creek trondhjemites and, most likely, the Brandy Not Granite, a series of I-type plutons (Champion, 1991). The westernmost granites in the Georgetown Inlier, the Esmeralda Supersuite, are generally classified as S-type due to their peraluminous nature, the abundance of muscovite and biotite (\pm garnet) and their reduced state. However, Budd et al. (2001) suggested that parts of the Esmeralda Supersuite could be classed as I-type because some samples contain hornblende and several of the granites are oxidized. Graphitic sedimentary xenoliths are common, and assimilation of such material by the magma may have produced the reduced granites of the supersuite and their peraluminous geochemistry.

2.3 Empress Springs Project

The Empress Springs Project comprises eleven tenements (EPM 25208–25210 [shown on Fig. 1b], EPM27193–27200 [not shown on Fig. 1b]) with a total area of 2386 km², approximately ~20 km southwest of the Georgetown Inlier (Fig. 1a). The tenements overlay a lithospheric-scale structural discontinuity that is observed in a deep seismic reflection line that penetrates down to the Moho (Fig. 1c, d; Moho Resources, 2019b), which is approximately where Pourteau et al. (2018) interpreted the suture between the Mount Isa and Georgetown Inliers. At the surface, this structural continuity is manifested as several major N–S and NW–SW striking faults that are resolved in aeromagnetic images (Fig. 1b; Moho Resources, 2019b). It is likely that the highly tectonized crust (Fig. 1b) records multiple second and third order antithetic and synthetic faults similar to what is shown further west of the Empress Springs Project in the seismic data (Fig. 1c, d). Thus, any potential mineralizing fluids generated during or after the suture event may have used a structural pathway from the upper mantle to the upper crust.

Reconnaissance air core and reverse circulation drilling was conducted in the Empress Springs Project in 2018, which revealed anomalous precious metal and base metal mineralization at the Arrowhead prospect (Moho Resources, 2019d). Further drilling in early to mid-2019 extended lateral and vertical mineralization at Arrowhead and identified two other precious- and base metal-enriched regions (Yappar and Wilson Bore prospects) along the southern edge of what is interpreted as a Proterozoic caldera structure, although no age constraints currently exist (Fig. 1b; Moho Resources, 2019a; Moho Resources, 2019c).

The basement of the Empress Springs project is situated under ~50 m of Phanerozoic cover and comprises variably altered porphyritic granite (*sensu lato*), intermediate to felsic volcanic rocks, mafic intrusions, and sedimentary rocks (Fig. 2; Moho Resources, 2019d). Alteration is composed of quartz–sericite (\pm chlorite), chlorite–biotite and minor disseminated pyrite (Moho Resources, 2019c, d). Units strike N to NW at the Arrowhead prospect and are steeply-dipping to the east (Moho Resources, 2019a).

3 METHODS

3.1 Sample acquisition and preparation

The Empress Springs Project exploration programme is still in its early stages, with the samples presented in this paper taken from the first set of drill holes conducted in the region. Although diamond drilling is the preferred mechanism to obtain core free of contaminants, it is prohibitively costly in the early stages of an exploration programme. Therefore, cheaper alternatives such as air core or reverse circulation are best employed to extract rock cuttings. These techniques are prone to contamination from loose sediment caving in from further up-hole and surface sediment during sampling. Nonetheless, chip cuttings are virtually the only cost-effective medium on which to obtain scientific information early in a mineral exploration programme.

Ten representative samples were selected from various prospects and lithologies around the Empress Springs Project (Table 1, Fig. 1b). All samples were dated by zircon U-Pb geochronology. Two of the samples (ESA023, 53–54m [syenogranite], and ESR022, 59–60m [andesite]) were also selected for sericite $^{40}\text{Ar}/^{39}\text{Ar}$ dating.

To minimize contamination of chip cuttings with other fine-grained material introduced during drilling and sampling, all ten samples were first washed and sieved to $>750\ \mu\text{m}$. Fractions $<750\ \mu\text{m}$ were discarded. We note, however, that a small portion of the $>750\ \mu\text{m}$ particles were clumps of drilling mud that probably had smaller particles embedded in them. Thus, although care was taken to mitigate contaminants from the investigated depths, some components from the up-hole lithologies are possibly present in the samples.

3.2 Thin section preparation and analysis

Thin sections were prepared from representative rock chips for each sample by Minerex Petrographic Services Ltd, Kalgoorlie, Western Australia. Thin sections were subsequently carbon coated and analyzed using a Tescan Integrated Mineral Analyser (TIMA) in the John de Laeter Centre (JdLC),

Curtin University, to aid in mineral identification. A TIMA (a field emission gun scanning electron microscopy) is equipped with four electron dispersive X-ray spectrometers (EDS), capable of recording 420k X-ray counts per second. Thin sections were analyzed in ‘dot-mapping’ mode with a rectangular mesh at a step-size of 3 μm for backscattered electron (BSE) imaging. One thousand EDS counts are collected every 9th step (i.e., 27 μm) or when the BSE contrast changes (i.e., a change in mineral phase). For a given mineral grain, EDS counts are integrated across the entire grain. TIMA analyses used an accelerating voltage of 25 kV, a beam intensity of 19, a probe current of 6.74–7.01 nA, a spot size of 67–90 nm and a nominal working distance of 15 mm. After imaging and EDS collection, BSE signals and EDS peaks are referenced to a mineral library for automatic mineral classification.

3.3 Sample processing and grain imaging

Samples >750 μm were disaggregated using the Selving high-voltage pulse fragmentation system in the JdLC, Curtin University, to liberate their constituent minerals. Resultant slurries were run through a Jasper Canyon Research concentrating shaker table for initial concentration of heavy minerals and subsequently through LST heavy liquids at 2.9 g cm^{-3} . The heavy fraction was run through a Frantz isodynamic magnetic separator.

For magmatic samples (Table 1), the non-magnetic heavy fractions were hand-picked for the highest quality zircon grains, which were mounted in 25 mm epoxy rounds. For the sedimentary sample (Table 1), no grain picking was employed to mitigate bias, and all non-magnetic grains from the heavy fraction were mounted in a 25 mm diameter mount. All mounts were polished to half-grain thickness to expose their interiors. Mounted grains were imaged with transmitted and reflected light on a Zeiss Axio Imager 2 optical microscope and, subsequently, with cathodoluminescence (CL) imaging using a Tescan Mira3 FEG-SEM at the JdLC at Curtin University. Transmitted and reflected light images were used to assess grain shape and transparency. Cathodoluminescence images were used to document internal zonation patterns (e.g. oscillatory, sector) and identify growth and recrystallization textures (e.g., Corfu et al., 2003; Olierook et al., 2020b). A full compendium of CL

images may be found in Supplementary Fig. A. For the magmatic samples, U-Pb spots were pre-selected to avoid inclusions, cracks and core-rim mixtures. For the sedimentary sample, analyses were conducted targeting sufficient grains to capture minor subpopulations without preselecting grains, in order to minimize sample bias and yield an objective detrital zircon distribution (e.g., Olierook et al., 2020a; Vermeesch, 2004).

For the two sericite samples (Table 1), the light fractions were sieved to 125–212 μm , subjected to a Nd-Fe-B magnet and magnetically separated using a Frantz magnetic separator. The non-magnetic fraction was handpicked for ~50 white, opaque grains of sericite per sample (e.g., Olierook et al., 2017; Verati and Jourdan, 2014).

3.4 Zircon U-Pb geochronology

Zircon U-Pb measurements were collected across two sessions at the GeoHistory Facility, JdLC, Curtin University. Where possible, spots were collected from both grain cores and rims. For both sessions, the excimer laser (RESOLUTION LR 193 nm ArF with a Lauren Technic S155 cell) beam diameter was 30 μm , on-sample energy was 2.3 J cm^{-2} with a repetition rate of 7 Hz for 45 s of analysis time and ~60 s of background capture. All analyses were preceded by three cleaning pulses. The sample cell was flushed by ultra-high purity He (0.68 L min^{-1}) and N_2 (2.8 mL min^{-1}).

U-Pb data were collected on an Agilent 7700s quadrupole mass spectrometer for session 1 and on an Agilent 8900 triple quadrupole mass spectrometer for session 2 with high purity Ar as the carrier gas for both sessions (flow rate 0.98 L min^{-1}). Analyses of 10 unknowns were bracketed by analysis of a standard block containing the primary zircon reference materials 91500 ($1062.4 \pm 0.4 \text{ Ma}$; Wiedenbeck et al., 1995) and OG1 ($3465.4 \pm 0.6 \text{ Ma}$; Stern et al., 2009), which were used to monitor and correct for mass fractionation and instrumental drift. The standard block also contained a range of secondary zircon standards spanning Archean to Phanerozoic ages, including Plešovice ($337.13 \pm 0.37 \text{ Ma}$; Sláma et al., 2008), GJ-1 ($601.95 \pm 0.40 \text{ Ma}$; Horstwood et al., 2016; Jackson et al., 2004) and Maniitsoq ($3008.70 \pm 0.72 \text{ Ma}$; Marsh et al., 2019; all uncertainties at 2σ), which were used to monitor data accuracy and precision. During the analytical sessions, when reduced against a matrix-

matched reference material, Plešovice, GJ-1 and Maniitsoq yielded statistically-reliable ($p > 0.05$) weighted mean ages of 336.72 ± 0.84 to 338.3 ± 1.0 Ma, 602.9 ± 1.7 to 604.4 ± 2.9 and 3007 ± 8 to 3010 ± 8 Ma, respectively, all of which are within 2σ of the published age (see supplementary Table A for full U-Pb compilation, including standards).

Data were reduced in Iolite3 (Paton et al., 2011) and in-house Excel macros. Zircon analyses are considered concordant where the error ellipses at 2σ generated by the $^{207}\text{Pb}/^{206}\text{Pb}$ and $^{206}\text{Pb}/^{238}\text{U}$ ratios overlap the inverse concordia curve, excluding uncertainties on the decay constant (i.e., assuming the concordia curve is a line rather than a zone). Uncertainties on the primary reference materials were propagated in quadrature to the unknowns and secondary zircon reference materials. Age calculations and plots utilized Isoplot 4.15 software (Ludwig, 2012). Full isotopic data for the samples are given in supplementary Table A. All zircon dates older than 1500 Ma are presented as $^{207}\text{Pb}/^{206}\text{Pb}$ ages and dates younger than 1500 Ma are presented as $^{206}\text{Pb}/^{238}\text{U}$ ages (Spencer et al., 2016). Common-Pb was not corrected for as almost all concordant analyses have apparent $f_{206\%} < 0.1\%$ (supplementary Table B). All spot analyses are presented at 2σ and weighted mean analyses are presented at 95% confidence.

3.5 $^{40}\text{Ar}/^{39}\text{Ar}$ geochronology

Handpicked sericite fractions were loaded into several small wells in 1.9 cm diameter and 0.3 cm depth aluminium discs. The discs were Cd-shielded (to minimize undesirable nuclear interference reactions) and irradiated for 40 hours in the TRIGA nuclear reactor (Oregon, USA) in central position. A single sericite grain was analyzed from both samples, with the remaining irradiated grains kept in reserve.

The $^{40}\text{Ar}/^{39}\text{Ar}$ analyses were performed on an ARGUS VI at the Western Australian Argon Isotope Facility at Curtin University. The ages were calculated using GA1550 biotite neutron flux monitor, for which an age of 99.738 ± 0.104 Ma (1σ) was used (Renne et al., 2011). The mean J-values computed from standard grains are $0.01078330 \pm 0.00000485$ (0.04%, 1σ), determined as the average and standard deviation of J-values of the small wells for the irradiation disc. Mass discrimination was

monitored using an automated air pipette and provided a mean value of 0.99382 ± 0.00089 (0.09%, 1σ) per dalton. The correction factors for interfering isotopes were $(^{39}\text{Ar}/^{37}\text{Ar})_{\text{Ca}} = 6.95 \times 10^{-4}$ ($\pm 1.3\%$, 1σ), $(^{36}\text{Ar}/^{37}\text{Ar})_{\text{Ca}} = 2.65 \times 10^{-4}$ ($\pm 0.8\%$, 1σ) and $(^{40}\text{Ar}/^{39}\text{Ar})_{\text{K}} = 7.30 \times 10^{-4}$ ($\pm 12\%$, 1σ).

The criteria for the determination of plateaus are as follows: (i) plateaus must include at least 70% of ^{39}Ar , and (ii) the plateaus should be distributed over a minimum of three consecutive steps agreeing at 95% confidence level and satisfying a probability of fit (p) of at least 0.05 (Merle et al., 2019; Olierook et al., 2019; Olierook et al., 2016). Plateau ages are given at the 2σ level and are calculated using the mean of all the plateau steps, each weighted by the inverse variance of their individual analytical error. All known sources of uncertainty are included in the calculation. Full $^{40}\text{Ar}/^{39}\text{Ar}$ data tables may be found in Supplementary Table B.

3.6 Whole-rock major and trace element geochemistry

All samples were trimmed to remove regolith crust and a subset sent to ALS Global (Perth) for major and trace element analysis. The samples were crushed using a jaw crusher and pulverized using a low-chrome steel mill to yield particles with size $< 75 \mu\text{m}$. To determine major and most trace element concentrations, a prepared aliquot (25 g) was weighed directly into a Teflon beaker and a concentrated aqua regia digest (1:3 ratio of concentrated HNO_3 to HCl) was added. The samples were placed on a hotplate at 200°C and evaporated until dry. The residue was then re-dissolved in 10% v/v HCl and returned to the hotplate at 100°C . When the residue was completely dissolved, the samples were cooled and transferred to 50 ml storage tubes. One ml of 0.5% w/v H_3BO_3 was added to each tube to complex HCl and mitigate ICP degradation. Most elements were analyzed by inductively coupled plasma atomic emission spectroscopy (ICP-AES; ME-ICP43 code in Supplementary Table C) or inductively coupled plasma mass spectrometry (ICP-MS; ME-MS43 and ME-TL43 [Au only] codes in Supplementary Table C) using a single-collector quadrupole. Results were subsequently corrected for spectral inter-element interferences.

Due to the low detection limit of Au, 50g aliquots of thirty-three selected samples were re-analyzed using a high-temperature litharge (PbO) fire assay flux (Au-AA22 for most and Au-AA26 for three

intervals from ESA023). Once cooled, the flux was measured using atomic absorption spectroscopy (AAS). The primary difference between Au-AA22 and -26 are their detector counting times, and their detection limits of 0.001–10 ppm and 0.1–100 ppm, respectively. Au-AA26 was chosen for the basal three intervals from ESA023 (48–50 m, 50–52 m and 52–54 m) due to the possibility of exceeding the upper limit of detection with Au-AA22.

4 RESULTS

4.1 Sample descriptions

Four granite samples were selected, one from each prospect (Table 1, Fig. 3a–d), comprising a syenogranite, and three monzogranites. Sample ESA023, 48–54m is a medium-grained syenogranite from the Arrowhead East prospect. It comprises mostly quartz (both primary and secondary), sericite and K-feldspar, with minor biotite and plagioclase and accessory apatite, pyrite, sphalerite and galena (Fig. 3a, Table 1). Samples ESR001, 95–96m and ESR054, 54–55m are coarse-grained monzogranites from the Fishhooks and Laneway South prospects, respectively. They comprise predominantly sericitized plagioclase, perthitic K-feldspar and quartz, with minor chloritized biotite, and rare calcite, apatite, fluorite and monazite (Fig. 3b, c, Table 1). Sample ESR015, 67–68m is a pyrite-rich monzogranite from the Racetrack prospect. Two individual chips were analyzed, with one showing similar mineral compositions and proportions to the other monzogranite samples (verging on granodiorite compositions), albeit with significant amounts of pyrite (top of Fig. 3d, Table 1). The other chip shows a pyrite-, kaolinite- and illite-rich vein that cross-cuts the host monzogranite (bottom of Fig. 3d, Table 1).

Four intermediate to felsic volcanic rocks were selected, comprising andesite, dacite and two rhyolites (Table 1, Fig. 3e–h). Sample ESR041, 63–64m is a sparsely-amygdaloidal porphyritic rhyolite from the Arrowhead prospect. It consists of phenocrysts of plagioclase, quartz and K-feldspar, enclosed in a groundmass of the same three minerals and additional chlorite and fluorite (Fig. 3e, Table 1). Sample ESR022, 59–60m is a pervasively altered, very fine- to fine-grained andesite from the Racetrack

prospect. The investigated chip contains two discrete parts, potentially reflecting a flow boundary (Fig. 3f). The lower part of the chip (upper part of older flow) is very-fine grained and comprises chiefly sericite, illite/smectite and chlorite, with minor pyrite, hematite, K-feldspar and quartz (Fig. 3f). The upper portion of the chip (lower part of younger flow) is fine-grained and comprises K-feldspar, illite/smectite, hematite and quartz (Fig. 3f). Sample ESR028, 64–65m is a microporphyritic rhyolite from the Arrowhead prospect. It comprises plagioclase and quartz glomerocrysts, with a groundmass of sericitized plagioclase, quartz and K-feldspar, with rare kaolinite (Fig. 3g, Table 1). Sample ESA014 is a dacite from the Fishhooks prospect. It comprises partly sericitized plagioclase, K-feldspar, quartz and chlorite, with minor rutile, apatite and pyrite (Fig. 3g, Table 1).

One equigranular dolerite sample (ESR011, 72–73m) was selected from the Racetrack prospect. It comprises predominantly plagioclase and clinopyroxene, and minor actinolite, secondary quartz, chlorite, smectite and sericite (Fig. 3i, Table 1).

One fine- to medium-grained quartzite sample (ESA012, 55–56m) was selected from the Fishhooks prospect. This quartzite sample comprises chiefly subangular to subrounded quartz and minor orthoclase grains, with pore space occluded by secondary kaolinite and illite (Fig. 3j, Table 1).

4.2 Zircon textures and U-Pb data

4.2.1 Granites

Zircon grains from the granites are euhedral to subhedral, 80–200 μm long, and have aspect ratios of 1:1 to 2:1 (Fig. 4a, b, Supplementary Fig. A). There is no significant textural difference between zircon grains from the syenogranite and the monzogranite samples, with both displaying weak to moderately-well developed oscillatory and rarer sector-zoning. Zircon grain cores and thick, oscillatory-zoned mantles are relatively common (Fig. 4a, b). One grain from sample ESR054, 54–55m (spot 14, Fig. 4b) is longer and larger than all other dated grains and is brighter in CL with two very broad zones.

All four granite samples yielded dominantly unimodal zircon age fractions at ca. 1560–1550 Ma, with rare analyses between 1720 and 1600 Ma (Fig. 5). Five concordant analyses younger than ca. 1500 Ma were encountered (see Fig. 5e and 5g), which are considered to have been derived from the up-hole stratigraphy (see section 6.1).

For concordant analyses only, syenogranite sample ESA023, 53–54m from the Arrowhead prospect yielded a $^{207}\text{Pb}/^{206}\text{Pb}$ weighted mean age of 1561 ± 10 Ma ($n = 7$, $\text{MWS} = 1.09$, $p = 0.36$, Fig. 5b). Monzogranite sample ESR001, 95–96m from the Fishhooks prospect yielded a $^{207}\text{Pb}/^{206}\text{Pb}$ weighted mean age of 1558 ± 5 Ma ($n = 28$, $\text{MWS} = 0.47$, $p = 0.99$, Fig. 5d). Monzogranite sample ESR054, 54–55m from the Laneway South prospect yielded a $^{207}\text{Pb}/^{206}\text{Pb}$ weighted mean age of 1559 ± 6 Ma ($n = 18$, $\text{MWS} = 0.58$, $p = 0.91$, Fig. 5f). Pyrite-rich monzogranite sample ESR015, 67–68m from the Racetrack prospect yielded a $^{207}\text{Pb}/^{206}\text{Pb}$ weighted mean age of 1564 ± 6 Ma ($n = 33$, $\text{MWS} = 0.53$, $p = 0.99$, Fig. 5h). All available ages from granite samples overlap at the 95% confidence level.

4.2.2 Volcanic rocks

Zircon grains from the volcanic rocks are euhedral to anhedral, 80–200 μm long and have aspect ratios of 1:1 to 3:1 (Fig. 4c–e, Supplementary Fig. A). Grains attributed to Group I and X have weak to moderately-well developed oscillatory- and sector-zoning. Grains belonging to Group C have variable internal textures (including well-developed oscillatory zoning or mottled zoning) or are exceptionally bright in CL (Fig. 4c, d). For Group C, grain cores are also common, but cores and rims are rare in Groups I and X.

The U-Pb data for the volcanic rocks are highly variable. Two of the four samples (ESA014, 51–52m [dacite] and ESR022, 59–60m [andesite]) exhibit a cluster at ca. 1560 Ma related to Group I (Fig. 6). Three of the four samples (except andesite sample ESR022, 59–60m) yielded a spread of U-Pb dates between ca. 600 and 250 Ma related to Group C (Fig. 6). These younger dates are considered to represent zircon grains from the overlying stratigraphy, either introduced during drilling or from sample collection (see Section 5.1). Grains from Group C are not considered for further analysis.

Using concordant analyses only, dacite sample ESA014, 51–52m from the Fishhooks prospect yielded a $^{207}\text{Pb}/^{206}\text{Pb}$ weighted mean age of 1546 ± 13 Ma ($n = 4$, MWSD = 0.93, $p = 0.42$, Fig. 6d). Andesite sample ESR022, 59–60m from the Racetrack prospect yielded a $^{207}\text{Pb}/^{206}\text{Pb}$ weighted mean age of 1560 ± 5 Ma ($n = 33$, MWSD = 0.31, $p = 1.00$, Fig. 6f). The only concordant analyses from rhyolite samples ESR041, 63–64m and ESR028, 64–65m are from the up-hole stratigraphy (Fig. 6a, b), and thus no age is calculated for these two samples. All available ages from volcanic samples overlap at 95% confidence.

4.2.3 Dolerite

Zircon grains from sample ESR011-36 are euhedral to anhedral (70–200 μm long and have aspect ratios of 2:1 to 5:1 (Fig. 4f, Supplementary Fig. A). The majority of grains are relatively dark in CL with faint oscillatory- or sector-zoning (Groups I and X in Fig. 4f), but a subordinate proportion was brighter in CL, with more distinct oscillatory- and sector-zoning (Group C in Fig. 4f).

Like some of the volcanic rocks, the U-Pb data show a cluster of ca. 1560 Ma grains as well as younger Phanerozoic ages (Fig. 7a). The latter is likewise interpreted as being derived from the up-hole stratigraphy and excluded from further discussion (see Section 5.1). Except for one concordant analysis at ca. 1760 Ma that is probably inherited, dolerite sample ESR011, 72–73m from the Racetrack prospect yielded a $^{207}\text{Pb}/^{206}\text{Pb}$ weighted mean age of 1560 ± 7 Ma ($n = 14$, MWSD = 0.33, $p = 0.98$, Fig. 7b).

4.2.4 Sedimentary sample

Zircon grains were abundant in quartzite sample ESA012, 53–54m (Supplementary Fig. A). They are angular to subrounded, 50–150 μm in diameter, with aspect ratios from 1:1 to 4:1 (Fig. 4g, Supplementary Fig. A). Rims are extremely rare (Supplementary Fig. A). The majority of grains exhibited oscillatory- or sector-zoning but with a clear bimodality concerning the brightness and definition of this zoning. A larger proportion of grains showed darker oscillatory zoning (Group S in Fig. 4g) compared to a subordinate fraction with brighter zoning (Group C in Fig. 4g).

The quartzite sample ESA012, 53–54m yielded a bimodal distribution of ages, with a major fraction at ca. 1560 Ma and a second Devonian subpopulation (Fig. 8a). Each subpopulation is linked to a mode of the bimodal CL zonation (Fig. 3g). The Devonian component is probably from the up-hole stratigraphy (see Section 5.1). Excluding the Devonian data, the U-Pb distribution is nearly unimodal around ca. 1560 Ma, with a rare component at ca. 1630 Ma (Fig. 8b).

4.3 Sericite $^{40}\text{Ar}/^{39}\text{Ar}$ data

Both samples from the Empress Springs Project yielded disturbed $^{40}\text{Ar}/^{39}\text{Ar}$ spectra with individual steps between ca. 330 and 250 Ma (Fig. 9). There is evidence for abundant excess radiogenic ^{40}Ar as shown by the particularly high $^{40}\text{Ar}/^{36}\text{Ar}$ of ~1,400–10,000 ($^{36}\text{Ar}/^{40}\text{Ar}$ intercepts of ~0.0001–0.0007; Fig. 9), an order of magnitude higher than the present-day atmospheric $^{40}\text{Ar}/^{36}\text{Ar}$ ratio of 298.56 ± 0.30 ($^{36}\text{Ar}/^{40}\text{Ar} = \sim 0.0033$; Lee et al., 2006).

4.4 Ore and pathfinder elements

In discovery hole ESA023, which shows the highest levels of Au (up to 2.1 ppm), various levels of precious metals (Ag, Au), base metals (Cu, Zn, Pb) and pathfinder elements (Hg, As, Sb, Te, W ± Bi, Mo) are anomalously elevated in five distinctly sampled intervals, with the three most enriched intervals shown in Fig. 10 (Supplementary Table C). Other elements such as the platinum group elements, Fe, Co, Ni, In, Tl, Sn, La and U are not enriched. Au/Ag ratios average ~1, ranging from 0.32–4.8. In ESR046, just south of ESR041 in the Wilson Bore Prospect at the edge of the caldera structure (Fig. 1b), the 63–65 m interval yielded almost 1 ppm Au by fire assay but with limited enrichments in other elements (Supplementary Table C).

For comparison to proximal deposits, the Empress Springs geochemical data in ESA023 are compared to three deposits with geochemical information in the Georgetown Inlier (Fig. 10). These include Croydon, an orogenic gold deposit associated with ca. 1.6 Ga Nuna assembly (Goldfarb et al., 2001; Partington and Williams, 2000), Einasleigh, a copper deposit of uncertain affinity but probably post-dating assembly at ca. 1.4 Ga (Evins et al., 2007; Patrick, 1978), and Kidston, a porphyry gold deposit associated with the Permo-Carboniferous orogeny in the Tasmanides of eastern Australia (Fig. 1b);

Perkins and Kennedy, 1998). Empress Springs shows significant affinity with Kidston, namely with elevated base metals (Cu, Zn, Cd, Pb), but lacks the pathfinder element peaks (As, Sb and Te) that Kidston shows (Fig. 10a). ESA023 shows little affinity with Croydon aside from precious metal similarities, and very little similarities exist between Empress Springs and Einasleigh (Fig. 10a).

For comparison to geochemically-similar deposits, several epithermal deposits around the world are contrasted to Empress Springs (Fig. 10b). These include Kelian (Indonesia) and Hidden Valley (Papua New Guinea), which are both Zn- and Pb-rich, low sulfidation epithermal gold deposits (Davies et al., 2008; Nelson et al., 1990; Van Leeuwen et al., 1990), and Equity (western Canada), which is an intrusion-related gold and silver epithermal deposit (Wojdak and Sinclair, 1984). Empress Springs shows strong similarities in terms of base metals (Cu, Zn, Cd, Pb), Au/Ag ratios (~1) but, like with Kidston, lacks some of the pathfinder elements peaks (As, Sb and Te).

5 DISCUSSION

5.1 Empress Springs Project – Glenmore or Mount Isa Inlier affinity?

Before assessing genetic links of the Empress Springs to basement inliers, it is first necessary to robustly classify the ages of measured samples. Zircon grains from the overlying succession may contribute to the post-1500 Ma zircon cargo in many samples and, despite washing and sieving mitigation procedures (see methods), is an unavoidable consequence of both the air core and reverse circulation sampling methods (Figs. 5–8). There are several pieces of evidence for this. (1) Based on drill hole cross-cutting relationships, the granites must be younger than, or at least contemporaneous with, the sampled volcanic and sedimentary rocks (Moho Resources, 2019d). Given that the granites yielded almost wholly zircon grains at ca. 1560–1550 Ma (86 of 94 concordant analyses, Fig. 5), the Phanerozoic zircon grains in some of the volcanic and sedimentary rocks cannot be *in situ* (Figs. 6–8). (2) All of the Phanerozoic cargo can be linked to the surrounding stratigraphy (see detailed compilation in Jell, 2013). For example, the largest subpopulation from the Carboniferous at ca. 343–317 Ma can be derived from the ca. 332 Ma Glenmore Supersuite, the ca. 339–332 Ma Kidston

Intrusions, the upper parts of the Gilberton Formation (ca. 331 Ma), the ca. 330 Ma Cumberland Volcanic Group and the lower parts of the Newcastle Range Volcanics (ca. 294 Ma). (3) The majority of the Phanerozoic grains are euhedral; thus, these zircon grains were probably minimally transported into the overlying sedimentary rocks to have preserved prismatic habits. All the above evidence suggests that the zircon grains are not endogenic to the dated samples but were instead introduced as contaminants from the drilling process.

The ages of the granites (1564 ± 6 Ma, 1561 ± 10 , 1559 ± 6 and 1558 ± 5 , Fig. 5), volcanic rocks (1560 ± 5 Ma and 1546 ± 13 and; Fig. 6) and mafic intrusions (1560 ± 7 Ma; Fig. 7) from the Empress Springs Project all overlap at 95% confidence and, thus, were all emplaced in a narrow time interval. A timeframe of ca. 1560–1550 Ma corresponds to the post-collisional stage of the 1600–1500 Ma Isan and Jana Orogenies that sutured the North Australian Craton and Laurentia, with granite emplacement occurring in both the Mount Isa (Mark, 2001; Page and Sun, 1998; Wyborn, 1998) and Georgetown Inliers (Black and McCulloch, 1990; Black and Withnall, 1993; Neumann and Kositsin, 2011). Despite temporal equivalence of granite emplacement across the region, there are key chemical and lithological differences between the granites in the Mount Isa and Georgetown Inliers. In Mount Isa, ca. 1550 Ma granites are mantle-derived, with tonalite–trondhjemite–granodiorite compositions (Mark, 2001; Page and Sun, 1998; Wyborn, 1998), whereas in the Georgetown Inlier, ca. 1560–1550 Ma granites are dominantly S-type, with an abundance of mica and paucity of hornblende (Black and McCulloch, 1990; Black and Withnall, 1993; Budd et al., 2001; Neumann and Kositsin, 2011). The Empress Springs granites are more akin to those in the Georgetown Inlier, with common biotite and muscovite, but hornblende absent (Table 1; Fig. 3). Thus, the age and composition of the granites at Empress Springs indicate that these probably belong to the Esmeralda Supersuite. One of the main characteristics of most (but not all) granites outcropping in the Georgetown Inlier is the presence of graphite. Of the 200 holes drilled to date by Moho Resources Ltd, around 130 intersected granite and none contained noticeable graphite. As none of the granites encountered at Empress Springs contains graphite, they may represent a different phase of the Esmeralda Supersuite or one of the other supersuites in the Georgetown Inlier.

The presence of coeval intermediate to felsic volcanic rocks at the Empress Springs Project is also consistent with this region being originally part of the Georgetown Inlier (Withnall et al., 2013).

Based on their composition and temporal equivalence, andesitic to rhyolitic lavas likely belong to the Croydon Volcanic Group, previously dated at 1548 ± 18 Ma (Black and Withnall, 1993). Volcanic rocks of this age are not recorded in the Mount Isa Inlier.

The sedimentary sequence encountered at Empress Springs indicates a unimodal population that was likely derived from the nearby Esmeralda Supersuite and Croydon Volcanic Group, notwithstanding that this interpretation is based off a single sample. The few older xenocrysts within the granitic rocks are also consistent with derivation from the underlying Etheridge Group (Furlanetto et al., 2016; Neumann and Kositcin, 2011; Nordsvan et al., 2018). The absence of significant proportions of younger grains (except those of Phanerozoic age) implies that this sedimentary unit is probably part of the ca. <1540 Ma Inorunie Group (Withnall et al., 2013), likely deposited shortly after cessation of magmatism in the Georgetown Inlier.

The above evidence from the granites, volcanic extrusions and sedimentary sequence indicates that the Empress Springs Project hosts rocks that are an extension of the Georgetown Inlier.

5.2 Age and genetic links to mineralization

The age of sericitization of plagioclase, potentially linked to gold mineralization at Empress Springs, cannot be robustly determined due to the disturbed $^{40}\text{Ar}/^{39}\text{Ar}$ spectra and the incorporation of significant excess radiogenic Ar (Fig. 9). Nonetheless, it is possible to make some broad interpretations of the likely age of sericitization. Incorporation of significant excess radiogenic Ar would make any apparent age older (Kelley, 2002), meaning that the ca. 300–250 Ma step dates could be considered a maximum age for the alteration of plagioclase to sericite (Fig. 9). One way of dealing with excess Ar is to use the inverse isochron but, in these samples, the measured Ar component is clustered and radiogenic and thus an inverse isochron cannot be accurately determined (Fig. 9b). Another consideration is whether further alteration or metamorphism occurred after sericitization that could have resulted in subsequent age resetting. The K/Ar (and $^{40}\text{Ar}/^{39}\text{Ar}$) system will provide the age

of the sericitization event once more than ~20–50% of the plagioclase has been converted to sericite due to the high to low K ratios of sericite and plagioclase, respectively (Verati and Jourdan, 2014). Thus, as long as the sericitization process was not protracted, which is unlikely in hydrothermal systems (Cathles et al., 1997; Chiaradia et al., 2013), the recorded alteration age should be geologically instantaneous, below the resolution of current $^{40}\text{Ar}/^{39}\text{Ar}$ instruments. Once nearly all the plagioclase has been transformed into sericite, the K/Ar clock will be likely locked in this state (Jourdan et al., 2009) unless the system is further altered to clay minerals, which is not evident. The presence of any reheating above the closure temperature of sericite (i.e., muscovite) during, for example, greenschist metamorphic conditions could lead to younger apparent ages, thereby making the true age of sericitization older. As there is no evidence for such conditions in the Empress Springs Project region in the Phanerozoic (e.g., Jell, 2013), the step dates around 330–250 Ma are considered a maximum age estimate for the sericitization event. The fact that two different samples yielded broadly comparable apparent step dates (Fig. 9) makes it likely that the age of sericitization is broadly around the ca. 330–250 Ma steps or younger.

Petrographic, geochemical and geochronological data all point toward an epithermal Au–Ag–Pb–Zn system. Ore and, to a lesser extent, pathfinder elements at Empress Springs show similar signatures to Kidston (Georgetown Inlier), Kelian (Indonesia), Hidden Valley (Papua New Guinea) and Equity (western Canada; Fig. 10). (ii) The presence of up to 0.25 wt. % Pb–Zn (Moho Resources, 2019d) together with Au/Ag ratios of ~1 is characteristic of epithermal gold systems (e.g., Hedenquist et al., 2000). The most common gangue minerals are quartz, calcite, adularia and illite, with pyrophyllite, alunite and barite absent (Fig. 3; Table 1), all of which point towards low rather than high-sulfidation state (i.e., reducing conditions; e.g., Hedenquist et al., 2000; White and Hedenquist, 1990). Although the ore minerals recovered at Empress Springs are not as diagnostic, the presence of ~0.1 wt. % sphalerite and galena in ESA023, 53–54m also hints at a low sulfidation system (Table 1). The fluids associated with crystallization of mafic and felsic volcanic rocks at ca. 1550 Ma, and/or Permo-Carboniferous hydrothermal fluids, both indicate that mineralization occurred after orogenesis associated with Nuna assembly, thereby precluding an orogenic gold system.

What remains uncertain is if the emplacement of mafic–felsic volcanic rocks at ca. 1550 Ma or whether the hydrothermal alteration ~1.3 b.y. after the assembly of Nuna was the primary driver for Au–Ag–Pb–Zn mineralization at Empress Springs. Both processes may have also been important, with the Permo-Carboniferous hydrothermal activity potentially upgrading earlier ca. 1550 Ma mineralization. Fluids expelled from mafic–felsic volcanic systems (particularly the more felsic end-members) are commonly associated with reducing fluids that can precipitate Au–Ag with sub-percent level Pb–Zn (John, 2001; Sillitoe and Hedenquist, 2003). Conversely, Permo-Carboniferous volcanic and/or intrusive equivalents have not (yet) been identified at the Empress Springs Project, so it is difficult to directly test if mineralization occurred at ca. 330–250 Ma.

To further evaluate a possible Permo-Carboniferous mineralization event, it is important to look slightly further afield from the Empress Springs Project in deposits that show a Permo-Carboniferous signature. Porphyry-style Cu–Au (e.g., Kidston, Buck Reef, Ravenswood, Mt Wright, Mt Leyshon deposits) has been documented from the Georgetown Inlier, and epithermal Au–Ag (Pajingo, Wirralie) just south of the Inlier, both thought to be associated with intruding granites during the Tasman orogenic system (Perkins and Kennedy, 1998). In particular, the ore and alteration assemblage at Ravenswood and Kidston show mineralogical, petrological and, for Kidston, geochemical affinities to the Empress Springs Project (Fig. 10; Neindorf et al., 1993; Perkins and Kennedy, 1998). $^{40}\text{Ar}/^{39}\text{Ar}$ dating from both these deposits show a similar stair-stepping sericite spectra, with the youngest apparent dates at ca. 260–250 Ma and the oldest at ca. 330 Ma (Perkins and Kennedy, 1998). Both gold deposits are porphyry-style systems and likely associated with contemporaneous microgranite intrusions at 335 ± 3 Ma (Perkins and Kennedy, 1998). Granite intrusions are commonly associated with gold mineralization (Haeussler et al., 1995; Lang and Baker, 2001; Thompson, 2000). It is common for epithermal (reducing) and porphyry-style (oxidizing) mineralization to occur contemporaneously and proximal to one another as part of a larger hydrothermal–magmatic system (Arribas Jr et al., 1995; Mao et al., 2011; Thiéblemont et al., 1997). Thus, epithermal sericitization and gold mineralization at Empress Springs may have been caused by the same larger-scale shallow magmatic system as the contemporaneous granite emplacement and

quartz–sericite alteration during the Permo-Carboniferous in other parts of the Georgetown Inlier. The caveat here is that Permo-Carboniferous granites have not been encountered in drill holes at Empress Springs, but intrusions of this age are known from the outcropping basement of the Georgetown Inlier (see detailed compilation in Jell, 2013) and present within the overlying sedimentary succession (see Group C zircon grains in Figs. 5–8).

5.3 Implications for the location and mineralization potential of the final Nuna suture

In several tectonic models, northeast Australia is located in the core of the supercontinent Nuna during the Proterozoic, implying it played an important role during its amalgamation (Kirscher et al., 2019; Pehrsson et al., 2016; Pisarevsky et al., 2014). However, there is still debate which suture zone (or zones) represents the final terrane boundary along the North Australian Craton and Laurentia. Possible suture zones observed in seismic reflection data include, from west to east, the (i) Gidyea Suture Zone (Betts et al., 2016; Korsch et al., 2012), (ii) a lithospheric-scale west-dipping fault that cross-cuts the Numil Seismic Province (here labelled as the Empress Suture Zone; Pourteau et al., 2018), and (iii) the Rowe Fossil Subduction Zone (Fig. 1c, d; Betts et al., 2016; Korsch et al., 2012). All these suture zones are west-dipping (Fig. 1c, d), implying that the North Australian terrane (Mount Isa Inlier) was the upper plate and Laurentia (Georgetown Inlier) was the lower plate. The Gidyea Suture Zone has been suggested to have formed due to the accretion of the Numil Seismic Province to the Mount Isa Inlier at ca. 1865 Ma (Korsch et al., 2012) but at least before ca. 1800 Ma based on overlying extensional basins (Betts et al., 2016). As such, the Gidyea Suture Zone is too old to be part of the final supercontinent building phase. Similarly, the Rowe Fossil Subduction Zone (Fig. 1c, d) is interpreted to form during an accretionary event between the Numil and Abingdon Seismic Provinces (Korsch et al., 2012) before deposition of the Etheridge Group at ca. 1700 Ma (Betts et al., 2016; Furlanetto et al., 2016; Neumann and Kositsin, 2011; Nordsvan et al., 2018). If the 1600–1500 Ma Isan/Jana Orogeny was not an intracontinental reworking event, then the Rowe Fossil Subduction Zone also cannot represent the final suturing of Nuna. Here, following Pourteau et al.,

(2018), we suggest that a lithospheric-scale west-dipping fault system that cross-cuts the Numil Seismic Province (here labelled as the Empress Suture Zone; Pourteau et al., 2018) records the final assembly of the North Australian Craton and Laurentia (Figs. 1, 11).

The interpretation that the Empress Suture Zone represents the final suture zone associated with the assembly of Nuna is supported by recent investigations of granites from drill holes situated under cover ~70 km southwest of the Empress Springs project (Nordsvan et al., in review). This study aimed to address a similar question—were these granites emplaced into crust more similar to the Mount Isa Inlier or the Georgetown Inlier, and does this narrow down the location of the suture zone? These granites, collectively termed the Cudjee Creek Granite, are classified as I-type, with significant hornblende and titanite ± allanite present in samples, and were dated at 1544 ± 5 and 1546 ± 4 Ma (Nordsvan et al., in review). The Cudjee Creek Granite was interpreted to be related to intrusions in the eastern belt of the Mount Isa Inlier given their similar composition and age (Fig. 11a). The findings imply that the final suture is likely situated between the position of the Cudjee Creek Granite and the Empress Springs region.

Seismic reflection data further constrain the possible suture location in the ~70 km-wide corridor between the Cudjee Creek Granite and Empress Springs Project. Importantly, there are no other lithospheric-scale structural discontinuities that penetrate down to the Moho between the Gidyea and Empress Suture Zones (Fig. 1c, d). The implication is that the Empress Suture Zone is the probable position of the final assembly of Nuna. However, the original interpretation of a narrow fault zone by Pourteau et al. (2018) is simplistic. We suggest that the west-dipping fault system that cross-cuts the Numil Seismic Province is at least ~10 km wide (Fig. 1c, d, Fig. 11) and is more likely to represent the scale of the Empress Suture Zone.

A sericitization and potential gold mineralization event occurring ~1.3 b.y. after host rock crystallization would attest to the long-lived reactivation potential of crustal-scale structural discontinuities (Fig. 11b). Re-activation of lithospheric-scale faults, especially suture zones, and mineralization along these conduits are common (Bao et al., 2017; Groves et al., 2010; Heinhorst et

al., 2000; Sarma et al., 2011). Several episodes of reactivation are also a common phenomenon, with upgrading of initial ore systems possible through pulses of fluid flow (Hart et al., 2002; Li et al., 2017; Pirajno and Bagas, 2002; Zheng et al., 2014; Zi et al., 2015). For example, initial ore deposition at the polymetallic Abra deposit in Western Australia formed at ca. 1590 Ma, but experienced reactivation at ca. 1380 Ma, 1220 Ma and 1000 Ma (Zi et al., 2015). Similarly, the northern margin of the North China Craton experienced up to four gold mineralization events between ca. 350 and 120 Ma (Goldfarb et al., 2019; Hart et al., 2002). Therefore, suture zones continue to be targeted for mineral exploration because of their ability to record multiple mineralizing and upgrading events through structural corridors. Irrespective of whether mineralization at Empress Springs occurred at ca. 1560–1550 Ma or 330–250 Ma (or both), the implication is that the position of the Empress Suture Zone (and any subsidiary, lower order structures) aided the transport of fluids to the shallow subsurface to form an epithermal system at the Empress Springs Project.

6 CONCLUSIONS

Zircon U-Pb dating of granites and volcanic rocks in the Empress Springs Project, NE Australia, reveals coeval emplacement and extrusions occurred between 1564 ± 6 and 1546 ± 13 Ma (2σ). The granite and volcanic rock ages correspond closely to the 1560–1550 Ma Esmeralda Supersuite and Croydon Volcanic Group, respectively, of the Georgetown Inlier, located ~20 km the northeast of the Empress Springs Project. Zircon U-Pb dating of a sedimentary rock revealed a near unimodal population at ca. 1560 Ma, probably corresponding to local derivation of granitic and volcanic rocks. All rock types are akin to rocks outcropping in the Georgetown Inlier. It is likely that a series of west-dipping lithospheric-scale faults below the Empress Springs Project, here termed the Empress Suture Zone, record the final suture zone associated with the assembly of Nuna (also known as Columbia) rather than lithospheric continuities further west or east. Sericite $^{40}\text{Ar}/^{39}\text{Ar}$ dating yielded disturbed spectra with evidence for incorporation of excess radiogenic Ar, with a probable Permian to Carboniferous age. Geochemical and age evidence points towards an epithermal system, with

hydrothermal activity (and mineralization) occurring at ca. 1560–1550 Ma and ca. 330–250 Ma.

Mineralization ~1.3 b.y. after crystallization indicates that metal-bearing fluids exploited permeable structural discontinuities long after initial fault formation. Ultimately, terrane-bounding suture zones continue to be important regions for mineral exploration.

The following are the supplementary data related to this article.

Supplementary Table A: U-Pb data for standards and unknown analyses. For Groups, C = contamination from the up-hole stratigraphy, D = discordant, I = magmatic, S = detrital, X = inherited.

Supplementary Table B: Full $^{40}\text{Ar}/^{39}\text{Ar}$ data tables.

Supplementary Table C: Whole-rock major and trace element data for drill hole intervals.

Supplementary Figure A: Compilation of all CL images for new samples.

Acknowledgements

This work was funded by Meko Resources Ltd. The John de Laeter Centre acknowledges operational funding for the GeoHistory and Argon Isotope Facilities provided by the AuScope Earth Composition and Evolution Program. The Australian Research Council is thanked for funding the Tescan Mira3 VP-FESEM (ARC LE130100053), Tescan Integrated Mineral Analyser (ARC LE1400100150), and the Selfrag HV pulse fragmentor (ARC LE130100219). We thank D. I. Groves for constructive comments and J. Meert for his editorial handling.

Declaration of interests

☒ The authors declare that they have no known competing financial interests or personal relationships that could have appeared to influence the work reported in this paper.

References

- Arribas Jr, A., Hedenquist, J.W., Itaya, T., Okada, T., Concepción, R.A., Garcia Jr, J.S., 1995. Contemporaneous formation of adjacent porphyry and epithermal Cu-Au deposits over 300 ka in northern Luzon, Philippines. *Geology* 23, 337-340.
- Baker, M.J., Crawford, A.J., Withnall, I.W., 2010. Geochemical, Sm–Nd isotopic characteristics and petrogenesis of Paleoproterozoic mafic rocks from the Georgetown Inlier, north Queensland: Implications for relationship with the Broken Hill and Mount Isa Eastern Succession. *Precambrian Research* 177, 39-54.
- Bao, Z., Sun, W., Zartman, R.E., Yao, J., Gao, X., 2017. Recycling of subducted upper continental crust: Constraints on the extensive molybdenum mineralization in the Qinling–Dabie orogen. *Ore Geology Reviews* 81, 451-465.
- Barrote, V., Tessalina, S., McNaughton, N., Jourdan, F., Hollis, S.P., Ware, B., Zi, J.-W., 2020. 4D history of the Nimbus VHMS ore deposit in the Yilgarn Craton, Western Australia. *Precambrian Research* 337, 105536.
- Betts, P.G., 1999. Palaeoproterozoic mid-basin inversion in the northern Mt Isa terrane, Queensland. *Australian Journal of Earth Sciences* 46, 735-748.
- Betts, P.G., Armit, R.J., Stewart, J., Aitken, A., Ailleres, L., Donchak, P., Hutton, L., Withnall, I., Giles, D., 2016. Australia and Nuna. 424, 47-81.
- Betts, P.G., Giles, D., 2006. The 1800–1100 Ma tectonic evolution of Australia. *Precambrian Research* 144, 92-125.
- Betts, P.G., Giles, D., Aitken, A., 2011. Paleoproterozoic accretion processes of Australia and comparisons with Laurentia. *International Geology Review* 53, 1357-1376.
- Bierlein, F.P., Maas, R., Woodhead, J., 2011. Pre-1.8 Ga tectono-magmatic evolution of the Kalkadoon–Leichhardt Belt: implications for the crustal architecture and metallogeny of the Mount Isa Inlier, northwest Queensland, Australia. *Australian Journal of Earth Sciences* 58, 887-915.
- Black, L.P., Gregory, P., Withnall, I.W., Bain, J.H.C., 1998. U–Pb zircon age for the Etheridge Group, Georgetown region, north Queensland: Implications for relationship with the Broken Hill and Mt Isa sequences. *Australian Journal of Earth Sciences* 45, 925-935.
- Black, L.P., McCulloch, M.T., 1990. Isotopic evidence for the dependence of recurrent felsic magmatism on new crust formation: An example from the Georgetown region of Northeastern Australia. *Geochimica et Cosmochimica Acta* 54, 183-196.
- Black, L.P., Withnall, I.W., 1993. The ages of Proterozoic granites in the Georgetown Inlier of northeastern Australia, and their relevance to the dating of tectonothermal events. *AGSO Journal of Australian Geology and Geophysics* 14, 331-341.
- Blaikie, T.N., Betts, P.G., Armit, R.J., Ailleres, L., 2017. The ca. 1740–1710Ma Leichhardt Event: Inversion of a continental rift and revision of the tectonic evolution of the North Australian Craton. *Precambrian Research* 292, 75-92.
- Blenkinsop, T.G., Huddleston-Holmes, C.R., Foster, D.R.W., Edmiston, M.A., Lepong, P., Mark, G., Austin, J.R., Murphy, F.C., Ford, A., Rubenach, M.J., 2008. The crustal scale architecture of the Eastern Succession, Mount Isa: The influence of inversion. *Precambrian Research* 163, 31-49.

- Boger, S.D., Hansen, D., 2004. Metamorphic evolution of the Georgetown Inlier, northeast Queensland, Australia; evidence for an accreted Palaeoproterozoic terrane? *Journal of Metamorphic Geology* 22, 511-527.
- Brauhart, C.W., Grunsky, E.C., Hagemann, S.G., 2017. Magmato-hydrothermal space: A new metric for geochemical characterisation of metallic ore deposits. *Ore Geology Reviews* 86, 867-895.
- Budd, A.R., Wyborn, L.A.I., Bastrakova, I.V., 2001. The metallogenic potential of Australian Proterozoic granites. *Geoscience Australia Record* 2001/12.
- Cathles, L.M., Erendi, A.H.J., Barrie, T., 1997. How long can a hydrothermal system be sustained by a single intrusive event? *Economic Geology* 92, 766-771.
- Cawood, P.A., Hawkesworth, C.J., 2015. Temporal relations between mineral deposits and global tectonic cycles. Geological Society, London, Special Publications 393, 9-21.
- Champion, D.C., 1991. The felsic granites of far north Queensland.
- Chiaradia, M., Schaltegger, U., Spikings, R., Wotzlaw, J.-F., Ovtcharova, M., 2013. How Accurately Can We Date the Duration of Magmatic-Hydrothermal Events in Porphyry Systems?—An Invited Paper. *Economic Geology* 108, 565-584.
- Cihan, M., Evins, P., Lisowiec, N., Blake, K., 2006. Time constraints on deformation and metamorphism from EPMA dating of monazite in the Proterozoic Robertson River Metamorphics, NE Australia. *Precambrian Research* 145, 1-23.
- Corfu, F., Hanchar, J.M., Hoskin, P.W.O., Kinny, P., 2003. Atlas of Zircon Textures. *Reviews in Mineralogy and Geochemistry* 53, 469-500.
- Davies, A.G.S., Cooke, D.R., Gemmell, J.B., van Leeuwen, T., Cesare, P., Hartshorn, G., 2008. Hydrothermal Breccias and Veins at the Kelian Gold Mine, Kalimantan, Indonesia: Genesis of a Large Epithermal Gold Deposit. *Economic Geology* 103, 717-757.
- Day, R.W., Whitaker, W.G., Murray, C.G., Wilson, H., Grimes, K.G., 1983. Queensland geology. A companion volume to the 1:2 500 000 scale geological map (1975). Geological Survey of Queensland, Publication 383.
- de Vries, S.T., Pryer, L.L., Fry, N., 2008. Evolution of Neoproterozoic and Proterozoic basins of Australia. *Precambrian Research* 166, 39-53.
- Deng, X.-D., Li, J.-W., Zhao, X.-F., Wang, H.-C., Qi, L., 2016. Re-Os and U-Pb geochronology of the Laochang Pb-Zn-Ag and concealed porphyry Mo mineralization along the Changning-Menglian suture, SW China: implications for ore genesis and porphyry Cu-Mo exploration. *Mineralium Deposita* 51, 237-248.
- Etheridge, M.A., Rutland, R.W.R., Wyborn, L.A.I., 1987. Orogenesis and tectonic process in the Early to Middle Proterozoic of northern Australia. *Proterozoic Lithospheric Evolution* 17, 131-147.
- Evins, P.M., Baker, T., Plakos, K.I., Giles, B., Williams, P.J., Lees, T., Gregory, P.W., Pearson, N.J., Selby, D., 2007. New geochronological constraints on the Einasleigh Cu deposit, Georgetown inlier, Queensland, Australia. *Society for Geology Applied to Mineral Deposits*, 389-392.
- Furlanetto, F., Thorkelson, D.J., Rainbird, R.H., Davis, W.J., Gibson, H.D., Marshall, D.D., 2016. The Paleoproterozoic Wernecke Supergroup of Yukon, Canada: Relationships to orogeny in northwestern Laurentia and basins in North America, East Australia, and China. *Gondwana Research* 39, 14-40.
- Geological Survey of Queensland, 2011. North-west Queensland Mineral and Energy Province Report. Department of Employment, Economic Development and Innovation.
- Gibson, G.M., Champion, D.C., Withnall, I.W., Neumann, N.L., Hutton, L.J., 2018. Assembly and breakup of the Nuna supercontinent: Geodynamic constraints from 1800 to 1600 Ma sedimentary basins and basaltic magmatism in northern Australia. *Precambrian Research* 313, 148-169.
- Gibson, G.M., Rubenach, M.J., Neumann, N.L., Southgate, P.N., Hutton, L.J., 2008. Syn- and post-extensional tectonic activity in the Palaeoproterozoic sequences of Broken Hill and Mount Isa and its bearing on reconstructions of Rodinia. *Precambrian Research* 166, 350-369.
- Giles, D., Betts, P., Lister, G., 2002. Far-field continental backarc setting for the 1.80–1.67 Ga basins of northeastern Australia. *Geology* 30, 823-826.
- Goldfarb, R., Qiu, K.-F., Deng, J., Chen, Y., Yang, L.J.E.G., 2019. Orogenic gold deposits of China.

- Goldfarb, R.J., Groves, D.I., Gardoll, S., 2001. Orogenic gold and geologic time: a global synthesis. *Ore Geology Reviews* 18, 1-75.
- Groves, D.I., Bierlein, F.P., 2007. Geodynamic settings of mineral deposit systems. *Journal of the Geological Society* 164, 19-30.
- Groves, D.I., Bierlein, F.P., Meinert, L.D., Hitzman, M.W., 2010. Iron Oxide Copper-Gold (IOCG) Deposits through Earth History: Implications for Origin, Lithospheric Setting, and Distinction from Other Epigenetic Iron Oxide Deposits. *Economic Geology* 105, 641-654.
- Groves, D.I., Goldfarb, R.J., Gebre-Mariam, M., Hagemann, S.G., Robert, F., 1998. Orogenic gold deposits: A proposed classification in the context of their crustal distribution and relationship to other gold deposit types. *Ore Geology Reviews* 13, 7-27.
- Haeussler, P.J., Bradley, D., Goldfarb, R., Snee, L., Taylor, C., 1995. Link between ridge subduction and gold mineralization in southern Alaska. *Geology* 23, 995-998.
- Hart, C.J., Goldfarb, R.J., Qiu, Y., Snee, L., Miller, L.D., Miller, M.L., 2002. Gold deposits of the northern margin of the North China Craton: multiple late Paleozoic- Mesozoic mineralizing events. *Mineralium Deposita* 37, 326-351.
- Hedenquist, J.W., Arribas, A., Gonzalez-Urien, E., 2000. Exploration for epithermal gold deposits. *Reviews in Economic Geology* 13, 45-77.
- Heinhorst, J., Lehmann, B., Ermolov, P., Serykh, V., Zhurutin, S., 2003. Paleozoic crustal growth and metallogeny of Central Asia: evidence from magmatic-hydrothermal ore systems of Central Kazakhstan. *Tectonophysics* 328, 69-87.
- Holcombe, R.J., Pearson, P.J., Oliver, N.H.S., 1991. Geometry of a Middle Proterozoic extensional décollement in northeastern Australia. *Tectonophysics* 191, 255-274.
- Horstwood, M.S.A., Košler, J., Gehrels, G., Jackson, S.E., McClean, N.M., Paton, C., Pearson, N.J., Sircombe, K., Sylvester, P., Vermeesch, P., Bowring, J.F., Condon, D.J., Schoene, B., 2016. Community-Derived Standards for LA-ICP-MS U-Th-Pb Geochronology – Uncertainty Propagation, Age Interpretation and Data Reporting. *Geostandards and Geoanalytical Research* 40, 311-332.
- Hou, Z., Duan, L., Lu, Y., Zheng, Y., Zhu, D., Yang, Z., Yang, Z., Wang, B., Pei, Y., Zhao, Z., 2015. Lithospheric architecture of the Lhasa terrane and its control on ore deposits in the Himalayan-Tibetan orogen. *Economic Geology* 110, 1541-1575.
- Jackson, M.J., Scott, D.L., Rawlings, D.J., 2000. Stratigraphic framework for the Leichhardt and Calvert Superbasins: review and correlations of the pre-1700 Ma successions between Mt Isa and McArthur River. *Australian Journal of Earth Sciences* 47, 381-403.
- Jackson, S.E., Pearson, N.J., Griffin, W.L., Belousova, E.A., 2004. The application of laser ablation-inductively coupled plasma-mass spectrometry to in situ U-Pb zircon geochronology. *Chemical Geology* 211, 47-69.
- Jell, P.A., 2013. *Geology of Queensland*. Geological Survey of Queensland.
- John, D.A., 2001. Miocene and Early Pliocene Epithermal Gold-Silver Deposits in the Northern Great Basin, Western United States: Characteristics, Distribution, and Relationship to Magmatism. *Economic Geology* 96, 1827-1853.
- Johnson, S.P., Thorne, A.M., Tyler, I.M., Korsch, R.J., Kennett, B.L.N., Cutten, H.N., Goodwin, J., Blay, O., Blewett, R.S., Joly, A., Dentith, M.C., Aitken, A.R.A., Holzschuh, J., Salmon, M., Reading, A., Heinson, G., Boren, G., Ross, J., Costelloe, R.D., Fomin, T., 2013. Crustal architecture of the Capricorn Orogen, Western Australia and associated metallogeny. *Australian Journal of Earth Sciences* 60, 681-705.
- Jourdan, F., Marzoli, A., Bertrand, H., Cirilli, S., Tanner, L.H., Kontak, D.J., McHone, G., Renne, P.R., Bellieni, G., 2009. $^{40}\text{Ar}/^{39}\text{Ar}$ ages of CAMP in North America: Implications for the Triassic-Jurassic boundary and the 40K decay constant bias. *Lithos* 110, 167-180.
- Kelley, S., 2002. Excess argon in K-Ar and Ar-Ar geochronology. *Chemical Geology* 188, 1-22.
- Kirscher, U., Liu, Y., Li, Z.X., Mitchell, R.N., Pisarevsky, S.A., Denyszyn, S.W., Nordsvan, A., 2019. Paleomagnetism of the Hart Dolerite (Kimberley, Western Australia) – A two-stage assembly of the supercontinent Nuna? *Precambrian Research* 329, 170-181.

- Korsch, R.J., Huston, D.L., Henderson, R.A., Blewett, R.S., Withnall, I.W., Fergusson, C.L., Collins, W.J., Saygin, E., Kositcin, N., Meixner, A.J., 2012. Crustal architecture and geodynamics of North Queensland, Australia: insights from deep seismic reflection profiling. *Tectonophysics* 572, 76-99.
- Lambeck, A., Barovich, K., Gibson, G., Huston, D., Pisarevsky, S., 2012. An abrupt change in Nd isotopic composition in Australian basins at 1655Ma: Implications for the tectonic evolution of Australia and its place in NUNA. *Precambrian Research* 208-211, 213-221.
- Lang, J.R., Baker, T., 2001. Intrusion-related gold systems: the present level of understanding. *Mineralium Deposita* 36, 477-489.
- Lee, J.-Y., Marti, K., Severinghaus, J.P., Kawamura, K., Yoo, H.-S., Lee, J.B., Kim, J.S., 2006. A redetermination of the isotopic abundances of atmospheric Ar. *Geochimica et Cosmochimica Acta* 70, 4507-4512.
- Li, W.-C., Yu, H.-J., Gao, X., Liu, X.-L., Wang, J.-H., 2017. Review of Mesozoic multiple magmatism and porphyry Cu–Mo (W) mineralization in the Yidun Arc, eastern Tibet Plateau. *Ore Geology Reviews* 90, 795-812.
- Lister, G.S., O'Dea, M.G., Somaia, I., 1999. A tale of two synclines: rift, inversion and transpressional popouts at Lake Julius, northwestern Mt Isa terrane, Queensland. *Australian Journal of Earth Sciences* 46, 233-250.
- Ludwig, K., 2012. User's manual for Isoplot version 3.75–4.15: a geochronological toolkit for Microsoft Excel. Berkeley Geochronological Center Special Publication.
- MacCready, T., Goleby, B.R., Goncharov, A., Drummond, B.J., Lister, G.S., 1998. A framework of overprinting orogens based on interpretation of the Mount Isa deep seismic transect. *Economic Geology* 93, 1422-1434.
- Mao, J., Zhang, J., Pirajno, F., Ishiyama, D., Su, H., Guo, C., Chen, Y., 2011. Porphyry Cu–Au–Mo–epithermal Ag–Pb–Zn–distal hydrothermal Au deposits in the Dexing area, Jiangxi province, East China—A linked ore system. *Ore Geology Reviews* 45, 203-216.
- Mark, G., 2001. Nd isotope and petrogenetic constraints for the origin of the Mount Angelay igneous complex: implications for the origin of intrusions in the Cloncurry district, NE Australia. *Precambrian Research* 105, 17-35.
- Marsh, J.H., Jørgensen, T.R.C., Petrus, J.A., Hamilton, M.A., Mole, D.R., 2019. U-Pb, trace element, and hafnium isotope composition of the Maniitsoq zircon: A potential new Archean zircon reference material, *Goldschmidt, Barcelona 2019*, 12-23 August, p. 2161.
- Meert, J.G., 2002. Paleomagnetic evidence for a Paleo-Mesoproterozoic supercontinent Columbia. *Gondwana Research* 5, 207-215.
- Meert, J.G., 2012. What's in a name? The Columbia (Paleopangaea/Nuna) supercontinent. *Gondwana Research* 21, 917-933.
- Meert, J.G., Santosh, M., 2017. The Columbia supercontinent revisited. *Gondwana Research* 50, 67-83.
- Merle, R.E., Jourdan, F., Chiaradia, M., Olierook, H.K.H., Manatschal, G., 2019. Origin of widespread Cretaceous alkaline magmatism in the Central Atlantic: A single melting anomaly? *Lithos* 342-343, 480-498.
- Moho Resources, 2019a. Broad zones of gold and base metals intersected at Empress Springs, ASX Announcement, 1 July 2019, <https://www.mohoresources.com.au/ASXReleasesQ32019>.
- Moho Resources, 2019b. Exploration update - Empress Springs, ASX Announcement, 28 May 2019, <https://www.mohoresources.com.au/ASXReleasesQ22019>.
- Moho Resources, 2019c. Moho discovers new gold mineralised systems at Empress Springs, ASX Announcement, 19 September 2019, <https://www.mohoresources.com.au/ASXReleasesQ32019>.
- Moho Resources, 2019d. Virgin gold & base metal discovery at Empress Springs, ASX Announcement, 7 February 2019, <https://www.mohoresources.com.au/ASXReleasesQ12019>.
- Neindorf, L., Dennis, R., Palmer, G., Clark, A., 1993. Ravenswood Gold Mine. An experience of rapid exploration, development and production. *Proceedings of North Queensland Gold '89 Conference, The Australasian Institute of Mining and Metallurgy, Melbourne*, pp. 115-125.

- Nelson, R.W., Bartram, J.A., Christie, M.H., 1990. Hidden Valley gold-silver deposit. *Geology of the Mineral Deposits of Australia and Papua New Guinea, 1773-1776*.
- Neumann, N., Kositsin, N., 2011. New SHRIMP U-Pb zircon ages from north Queensland, 2007-2010. *Geoscience Australia*.
- Nordsvan, A.R., Martin, E.L., Volante, S., Collins, W.J., Beams, S., Pourteau, A., Li, J., Withnall, I.W., Li, Z.-X., in review. New U-Pb ages and Lu-Hf isotope data from Mesoproterozoic granites in NE Australia. *Precambrian Research*.
- Nordsvan, A.R., Pourteau, A., Spencer, C.J., Volante, S., Collins, W.J., Li, Z.-X., Withnall, I.W., Betts, P.G., 2018. Laurentian crust in northeast Australia: Implications for the assembly of the supercontinent Nuna. *Geology* 46, 251-254.
- O'Dea, M.G., Betts, P.G., MacCready, T., Aillères, L., 2006. Sequential development of a mid-crustal fold-thrust complex: evidence from the Mitakoodi Culmination in the eastern Mt Isa Inlier, Australia. *Australian Journal of Earth Sciences* 53, 69-90.
- O'Dea, M.G., Lister, G.S., Betts, P.G., Pound, K.S., 1997a. A shortened intraplate rift system in the Proterozoic Mount Isa terrane, NW Queensland, Australia. *16*, 425-441.
- O'Dea, M.G., Lister, G.S., MacCready, T., Betts, P.G., Oliver, N.H.S., Pound, K.S., Huang, W., Valenta, R.K., Oliver, N.H.S., Valenta, R.K., 1997b. Geodynamic evolution of the Proterozoic Mount Isa terrain. *121*, 99-122.
- Olierook, H.K.H., Barham, M., Kirkland, C.L., Hollis, J., Vass, A., 2020a. Zircon fingerprint of the Neoproterozoic North Atlantic: perspectives from East Greenland. *Precambrian Research*, 105653.
- Olierook, H.K.H., Jiang, Q., Jourdan, F., Chiaradia, M., 2019. Greater Kerguelen large igneous province reveals no role for Kerguelen mantle plume in the continental breakup of eastern Gondwana. *Earth and Planetary Science Letters* 511, 244-255.
- Olierook, H.K.H., Jourdan, F., Merle, R.E., Timms, M.E., Kuszniir, N.J., Muhling, J., 2016. Bunbury Basalt: Gondwana breakup products or earliest vestiges of the Kerguelen mantle plume? *Earth and Planetary Science Letters* 440, 20-32.
- Olierook, H.K.H., Kirkland, C.L., Szilas, K., Hollis, J.A., Gardiner, N.J., Steenfelt, A., Jiang, Q., Yakymchuk, C., Evans, N.J., McDonald, B.L., 2020b. Differentiating between inherited and autocrystic zircon in granitoids. *Journal of Petrology*.
- Olierook, H.K.H., Merle, R.E., Jourdan, F., 2017. Toward a Greater Kerguelen large igneous province: Evolving mantle source contribution in and around the Indian Ocean. *Lithos* 282-283, 163-172.
- Olierook, H.K.H., Scalzo, R., Kohn, D., Chandra, R., Farahbakhsh, E., Clark, C., Reddy, S.M., Muller, R.D., In Press. Bayesian geological and geophysical data fusion for the construction and uncertainty quantification of 3D geological models. *Geoscience Frontiers*.
- Olierook, H.K.H., Sheppard, S., Johnson, S.P., Occhipinti, S.A., Reddy, S.M., Clark, C., Fletcher, I.R., Rasmussen, B., Zi, J.-W., Frazzno, F., LaFlamme, C., Do, T., Ware, B., Blandthorn, E., Lindsay, M., Lu, Y.-J., Crossley, R.J., Erickson, T.M., 2018. Extensional episodes in the Paleoproterozoic Capricorn Orogen, Western Australia, revealed by petrogenesis and geochronology of mafic-ultramafic rocks. *Precambrian Research* 306, 22-40.
- Page, R.W., Sun, S.S., 1998. Aspects of geochronology and crustal evolution in the Eastern Fold Belt, Mt Isa Inlier. *Australian Journal of Earth Sciences* 45, 343-361.
- Page, R.W., Williams, I.S., 1988. Age of the Barramundi Orogeny in northern Australia by means of ion microprobe and conventional U-Pb zircon studies. *Precambrian Research* 40, 21-36.
- Partington, G.A., Williams, P.J., 2000. Proterozoic lode gold and (iron)-copper-gold deposits: A comparison of Australian and global examples. *Reviews in Economic Geology* 13, 69-101.
- Paton, C., Hellstrom, J., Paul, B., Woodhead, J., Hergt, J., 2011. Iolite: Freeware for the visualisation and processing of mass spectrometric data. *Journal of Analytical Atomic Spectrometry* 26, 2508-2518.
- Patrick, J.P., 1978. The Geology and Origin of the Sulphide Deposit and the High Grade Precambrian Metamorphic Rocks at Einasleigh, Northeastern Australia.

- Pehrsson, S.J., Eglinton, B.M., Evans, D.A.D., Huston, D., Reddy, S.M., 2016. Metallogeny and its link to orogenic style during the Nuna supercontinent cycle. *424*, 83-94.
- Perkins, C., Kennedy, A.K., 1998. Permo-Carboniferous gold epoch of northeast Queensland. *Australian Journal of Earth Sciences* 45, 185-200.
- Pirajno, F., Bagas, L., 2002. Gold and silver metallogeny of the South China Fold Belt: a consequence of multiple mineralizing events? *Ore Geology Reviews* 20, 109-126.
- Pisarevsky, S.A., Elming, S.-Å., Pesonen, L.J., Li, Z.-X., 2014. Mesoproterozoic paleogeography: supercontinent and beyond. *Precambrian Research* 244, 207-225.
- Pourteau, A., Smit, M.A., Li, Z.-X., Collins, W.J., Nordsvan, A.R., Volante, S., Li, J., 2018. 1.6 Ga crustal thickening along the final Nuna suture. *Geology* 46, 959-962.
- Renne, P.R., Balco, G., Ludwig, K.R., Mundil, R., Min, K., 2011. Response to the comment by W.H. Schwarz et al. on "Joint determination of ^{40}K decay constants and $^{40}\text{Ar}^*/^{40}\text{K}$ for the Fish Canyon sanidine standard, and improved accuracy for $^{40}\text{Ar}/^{39}\text{Ar}$ geochronology" by PR Renne et al. (2010). *Geochimica et Cosmochimica Acta* 75, 5097-5100.
- Rudnick, R.L., Gao, S., 2003. Composition of the Continental Crust, In: Furekian, K.K. (Ed.), *Treatise on Geochemistry*. Pergamon, Oxford, pp. 1-64.
- Sarma, D.S., Fletcher, I.R., Rasmussen, B., McNaughton, N.J., Mohan, M.R., Groves, D.I., 2011. Archaean gold mineralization synchronous with late cratonization of the Western Dharwar Craton, India: 2.52 Ga U–Pb ages of hydrothermal monazite and xenotime in gold deposits. *Mineralium Deposita* 46, 273-288.
- Sillitoe, R.H., Hedenquist, J.W., 2003. Linkages between volcanic tectonic settings, ore-fluid compositions, and epithermal precious metal deposits. *Special Publication-Society of Economic Geologists* 10, 315-343.
- Sláma, J., Košler, J., Condon, D.J., Crowley, J.L., Górces, A., Hanchar, J.M., Horstwood, M.S.A., Morris, G.A., Nasdala, L., Norberg, N., Schaltegger, U., Schoene, B., Tubrett, M.N., Whitehouse, M.J., 2008. Plešovice zircon — A new natural reference material for U–Pb and Hf isotopic microanalysis. *Chemical Geology* 249, 1-35.
- Southgate, P.N., Neumann, N.L., Gibson, G.M., 2013. Depositional systems in the Mt Isa Inlier from 1800 Ma to 1640 Ma: Implications for Zn–Pb–Ag mineralisation. *Australian Journal of Earth Sciences* 60, 157-173.
- Spaggiari, C.V., Smithies, R.H., Kirkland, C.L., Wingate, M.T.D., England, R.N., Lu, Y.-J., 2018. Buried but preserved: The Proterozoic Archaic Ophiolite, Madura Province, Western Australia. *Precambrian Research* 317, 137-158.
- Spencer, C.J., Kirkland, C.L., Taylor, R.J.M., 2016. Strategies towards statistically robust interpretations of in situ U–Pb zircon geochronology. *Geoscience Frontiers* 7, 581-589.
- Stern, R.A., Bodorkos, S., Nimmo, S.L., Hickman, A.H., Corfu, F., 2009. Measurement of SIMS Instrumental Mass Fractionation of Pb Isotopes During Zircon Dating. *Geostandards and Geoanalytical Research* 33, 145-168.
- Thiéblemont, D., Stein, G., Lescuyer, J.-L., 1997. Epithermal and porphyry deposits: the adakite connection. *Comptes Rendus de l'Academie des Sciences Series IIA Earth and Planetary Science* 2, 103-109.
- Thompson, J.F.H., 2000. Gold deposits Related to Reduced granitic intrusion. *Society of Economic Geology Reviews* 13, 377-400.
- Tohver, E., Pluijm, B.A.v.d., Mezger, K., Scandolara, J.E., Essene, E.J., 2005. Two stage tectonic history of the SW Amazon craton in the late Mesoproterozoic: identifying a cryptic suture zone. *Precambrian Research* 137, 35-59.
- Van Leeuwen, T.M., Leach, T., Hawke, A.A., Hawke, M.M., 1990. The Kelian disseminated gold deposit, East Kalimantan, Indonesia. *Journal of Geochemical Exploration* 35, 1-61.
- Verati, C., Jourdan, F., 2014. Modelling effect of sericitization of plagioclase on the $^{40}\text{K}/^{40}\text{Ar}$ and $^{40}\text{K}/^{39}\text{Ar}$ chronometers: Implication for dating basaltic rocks and mineral deposits. *Geological Society Special Publication* 378, 155–174.

- Vermeesch, P., 2004. How many grains are needed for a provenance study? *Earth and Planetary Science Letters* 224, 441-451.
- Volante, S., Collins, W.J., Blereau, E., Pourteau, A., Spencer, C., Evans, N.J., Barrote, V., Nordsvan, A.R., Li, Z.X., Li, J., 2020a. Reassessing zircon-monzite thermometry with thermodynamic modelling: insights from the Georgetown igneous complex, NE Australia. *Contributions to Mineralogy and Petrology* 175, 110.
- Volante, S., Collins, W.J., Pourteau, A., Li, Z.-X., Li, J., Nordsvan, A.R., 2020b. Structural Evolution of a 1.6 Ga Orogeny Related to the Final Assembly of the Supercontinent Nuna: Coupling of Episodic and Progressive Deformation. *Tectonics* 39, e2020TC006162.
- Volante, S., Pourteau, A., Collins, W.J., Blereau, E.R., Li, Z.-X., Smit, M., Evans, N.J., Nordsvan, A.R., Spencer, C.J., McDonald, B.J., Li, J., Günter, C., In Press. Multiple P–T–d–t paths reveal the evolution of the final Nuna assembly in northeast Australia. *Journal of Metamorphic Geology*.
- White, N.C., Hedenquist, J.W., 1990. Epithermal environments and styles of mineralization: Variations and their causes, and guidelines for exploration. *Journal of Geochemical Exploration* 36, 445-474.
- Wiedenbeck, M., Allé, P., Corfu, F., Griffin, W.L., Meier, M., Oberli, F., Quadt, A.V., Roddick, J.C., Spiegel, W., 1995. Three natural zircon standards For U-Th-Pb, Lu-Hf, trace element And REE analyses. *Geostandards Newsletter* 19, 1-23.
- Withnall, I.W., 1996. Stratigraphy, structure, and metamorphism of the Proterozoic Etheridge and Langlovale Groups, Georgetown region, north Queensland. Australian Geological Survey Organisation.
- Withnall, I.W., Bain, J.H.C., Draper, J.J., MacKenzie, D.F., Oversby, B.S., 1988. Proterozoic stratigraphy and tectonic history of the Georgetown Inlier, north eastern Queensland. *Precambrian Research* 40-41, 429-446.
- Withnall, I.W., Hutton, L.J., Armit, R.J., Betts, P.C., Blewett, R.S., Champion, D.C., Jell, P.A., 2013. North Australian Craton, Geology of Queensland. Geological Survey of Queensland, pp. 23-112.
- Wojdak, P.J., Sinclair, A.J., 1984. Equity Silver silver-copper-gold deposit; alteration and fluid inclusion studies. *Economic Geology* 79, 965-990.
- Wyborn, L., 1998. Younger ca 1500 Ma granites of the Williams and Naraku Batholiths, Cloncurry district, eastern Mt Isa Inlier: geochemistry, origin, metallogenic significance and exploration indicators. *Australian Journal of Earth Sciences* 45, 397-411.
- Wyborn, L.A.I., Page, R.W., McCulloch, M.T., 1988. Petrology, geochronology and isotope geochemistry of the post-1820 Ma granites of the Mount Isa Inlier: mechanisms for the generation of Proterozoic anorogenic granites. *Precambrian Research* 40, 509-541.
- Zheng, Y., Sun, X., Gao, S., Zhao, Z., Zhang, G., Wu, S., You, Z., Li, J., 2014. Multiple mineralization events at the Jiru porphyry copper deposit, southern Tibet: Implications for Eocene and Miocene magma sources and resource potential. *Journal of Asian Earth Sciences* 79, 842-857.
- Zi, J.-W., Rasmussen, B., Muhling, J.R., Fletcher, I.R., Thorne, A.M., Johnson, S.P., Cutten, H.N., Dunkley, D.J., Korhonen, F.J., 2015. In situ U–Pb geochronology of xenotime and monazite from the Abra polymetallic deposit in the Capricorn Orogen, Australia: Dating hydrothermal mineralization and fluid flow in a long-lived crustal structure. *Precambrian Research* 260, 91-112.

Fig. 1: (a) Regional map of northeastern Australia, modified from Pourteau et al. (2018), showing the location of the Empress Springs Project tenements (black box) and proximal deposits with geochemical data (gold stars). Interpreted Nuna suture is from Pourteau et al. (2018). Simplified

position of seismic line 07GA-IG1 after Korsch et al. (2012). The Tasman line marks the boundary of cratonic Australia with Phanerozoic eastern Australia. NAC, SAC and WAC are North, South and West Australian Cratons, respectively. RFSZ = Rowe Fossil Subduction Zone. (b) Vertical derivative (1.5×) of total magnetic intensity, overlain with locations of Empress Springs Project tenements, drill holes (up to 2019) and prospects. Note that the aeromagnetic survey within the Empress Springs tenements was flown at 100 m line spacing (~25 m resolution) by Moho Resources, whereas the surrounding aeromagnetic survey (Australia-wide) was flown at 400 m line spacing (~100 m resolution). (c) Interpreted seismic section line 07GA-IG1, modified from Korsch et al. (2012). (d) Simplified seismic interpretation of 07GA-IG1, showing possible suture zone between Mount Isa and Georgetown Inliers (here termed the Empress Springs Suture Zone, see discussion), modified from Pourteau et al. (2018).

Fig. 2: Detailed map and cross-section across the eastern part of the Arrowhead Prospect, including discovery hole ESA023, modified from Moho Resources (2019b). (a) Map, showing vertical derivative (1.5×) of total magnetic intensity overlain with locations of Empress Springs Project drill holes (up to 2019), prospects and cadastral structure position. (b) Cross-section, showing elevated (<1g/t Au, orange) and highly elevated (>1g/t Au, red) levels of base metals and precious metals in the granodiorite and andesite.

Fig. 3: Automated mineral analysis maps of thin sectioned samples from samples of Empress Springs Project. Modal compositions may be found in Table 1. Note that the pyrite-rich monzogranite in (d) had two distinct rock chips that were considered as separate entities for modal mineralogy calculations in Table 1.

Fig. 4: Representative cathodoluminescence (CL) images of magmatic and detrital zircon grains from the Empress Springs Project. Circles (30 µm) correspond to analytical spot locations. Circle colours

correspond to genetic interpretation, used throughout other figures. Yellow = Group I, magmatic (igneous); red = Group X, inherited (xenocrystic); purple = Group S, detrital; white = Group C, concordant analyses considered to reflect contamination from the up-hole stratigraphy (strat.); black = Group D, discordant. A compilation of all CL images may be found in Supplementary Fig. A.

Fig. 5: Tera-Wasserburg inverse concordia plots and $^{207}\text{Pb}/^{206}\text{Pb}$ weighted mean ages for granites from the Empress Springs project. All uncertainties at 2σ .

Fig. 6: Tera-Wasserburg inverse concordia plots and $^{207}\text{Pb}/^{206}\text{Pb}$ weighted mean ages for volcanic rocks from the Empress Springs project. All uncertainties at 2σ .

Fig. 7: Tera-Wasserburg inverse concordia plot and $^{207}\text{Pb}/^{206}\text{Pb}$ weighted mean age for a dolerite from the Empress Springs project. All uncertainties at 2σ .

Fig. 8: Tera-Wasserburg inverse concordia plot and probability density plot for a quartzite from the Empress Springs project. All uncertainties at 2σ .

Fig. 9: (a, c) $^{40}\text{Ar}/^{39}\text{Ar}$ apparent age spectra and (b, d) inverse isochron for sericite separates from the Empress Springs Project. Individual steps are at 2σ uncertainty. See Supplementary Table B for full data.

Fig. 10: Comparison of geochemical data between Empress Springs and: (a) proximal gold deposits in the Georgetown Inlier, and (b) epithermal gold systems from around the world. All data are log normalized to upper continental crustal (UCC) values of Rudnick and Gao (2003), using the approach

of Ore Samples Normalised to Average Crustal Abundance (OSNACA; Brauhart et al., 2017). Log-values of 0 are at or below upper crustal values. Log-base values are 10 for most elements but, for clarity, selected abundant elements have base 9.57 (U), base 9.15 (Sn), base 8.58 (As), base 6.71 (Pb), base 6.07 (La) base 5.77 (Cr, Cu), base 5.07 (Ni), base 4.9 (Zn) base 1.6 (Fe). Chemical data for Croydon, Einasleigh and Kidston (all Georgetown Inlier), Kelian (Indonesia), Hidden Valley (Papua New Guinea) and Equity (western Canada) are from the OSNACA database (<http://www.cet.edu.au/projects/osnaca-ore-samples-normalised-to-average-crustal-abundance/>).

Fig. 11: Schematic summary of crystallization and mineralization history at the Empress Springs Project along the boundary of the former North Australian (Mount Isa Inlier) and Laurentian (Georgetown) terranes. (a) At ca. 1560–1550 Ma, coeval granite emplacement and volcanic extrusions occur (with minor mafic intrusions, not shown) in the former Laurentian terrane, with later, ca. 1540 Ma granite emplacement occurring in the former North Australian Craton. Possible associated epithermal gold mineralization may have occurred here associated with magmatic activity. (b) At ca. 330–250 Ma, renewed granite activity occurs with possible associated gold mineralization, potentially localized along the Empress Springs Suture Zone.

Table 1: Summary of analyzed samples. Modal mineralogy from automated mineral analysis (see Fig. 2). Note that ESR015, 67–68m had two distinct chips that were considered as separate entities (see Fig. 3d). Coordinates are GDA 1994, projected to Zone 54S.

Sample (Hole ID, Depth [m])	ESA 023, 53–54m	ESR 001, 95–96m	ESR 054, 54–55m	ESR 015, 67–68m	ESR 041, 63–64m	ESR 028, 64–65m	ESA 014, 51–52m	ESR 022, 59–60m	ESR 011, 72–73m	ESA 012, 55–56m
Lithology	Syeno-granite	Monzo-granite	Monzo-granite	Pyrite-rich vein Monzo-granite	Rhyolite	Rhyolite	Dacite	Andesite	Dolerite	Quartzite
Prospect	Arrowhead East	Fishhooks	Laneway South	Racetrack	Arrowhead	Arrowhead	Fishhooks	Racetrack	Racetrack	Fishhooks
Easting	633704	635592	627486	630858	628578	631853	636886	627484	629217	635872
Northing	7937052	7944543	7947622	7949227	7940432	7937716	7944486	7951603	7949813	7940797

Dated phases	Zircon, sericite	Zircon	Zircon	Zircon	Zircon	Zircon	Zircon	Zircon	Zircon, sericite	Zircon	Zircon
Quartz	51.47	23.16	24.86	22.90	17.58	29.44	28.11	5.27	2.70	3.74	78.13
K-feldspar (inc. adularia)	13.62	27.95	34.02	12.47	1.35	18.66	8.82	10.99	9.51	0.71	9.48
Plagioclase	0.52	37.52	27.46	44.46	0.05	42.74	39.51	16.65	0.56	35.94	0.16
Muscovite/sericite	23.91	2.99	3.21	8.33	1.83	0.14	6.73	1.46	2.00	1.02	1.70
Biotite	0.11	1.75	1.24	1.33	0.02	0.04	0.11	0.37	0.15	3.57	0.01
Chlorite	1.56	2.72	4.16	3.11	0.05	2.40	0.46	26.20	1.31	8.39	–
Kaolinite	0.01	0.02	0.19	0.45	7.05	0.04	0.61	0.23	0.21	–	5.69
Illite/illite-smectite	2.28	1.17	2.35	3.03	5.43	2.72	11.71	23.57	60.76	12.63	2.71
Smectite	–	–	–	–	–	0.01	–	0.12	–	2.07	–
Pargasite	–	0.01	–	–	–	–	–	0.01	–	1.30	–
Actinolite	–	–	–	–	–	–	–	–	–	5.96	–
Low-Ca pyroxene	–	–	–	–	–	–	–	0.01	–	1.13	–
Augite	0.01	0.21	0.44	0.43	0.00	0.45	0.18	0.94	–	12.38	–
Calcite	–	0.21	0.05	0.11	0.00	0.05	–	–	–	0.35	–
Fluorite	–	0.12	–	–	–	0.18	–	–	–	–	–
Barite	–	–	–	0.02	–	–	–	–	0.01	–	–
Apatite	0.20	0.20	0.11	0.17	0.00	0.02	–	1.10	–	0.40	–
Monazite	0.01	0.03	–	0.03	0.02	–	–	–	0.01	–	0.01
Zircon	–	0.03	0.03	0.04	0.02	0.01	–	–	–	–	0.08
Rutile	0.01	0.01	0.02	0.04	0.15	0.03	0.16	2.15	0.44	–	0.18
Titanite	–	–	–	–	–	–	–	–	–	0.80	–
Ilmenite	–	0.05	0.01	0.01	0.00	0.01	–	0.06	–	0.19	0.10
Fe-oxide	0.06	0.02	0.05	0.03	0.00	0.06	–	0.29	11.29	0.89	–
Pyrite	0.27	–	–	0.92	58.29	0.01	–	0.33	0.16	–	–
Pyrrhotite	–	–	–	0.20	–	–	–	–	–	–	–
Chalcopyrite	0.01	–	–	–	0.01	–	–	0.01	–	–	–
Sphalerite	0.09	–	–	–	–	–	–	–	–	–	–
Galena	0.11	–	–	–	–	–	–	–	–	–	–
Glue-resin	0.02	0.12	0.11	0.06	0.01	0.28	0.03	0.13	0.03	0.14	0.04
Unclassified	5.85	1.70	1.68	1.92	7.90	2.72	3.67	10.11	10.86	8.38	1.71

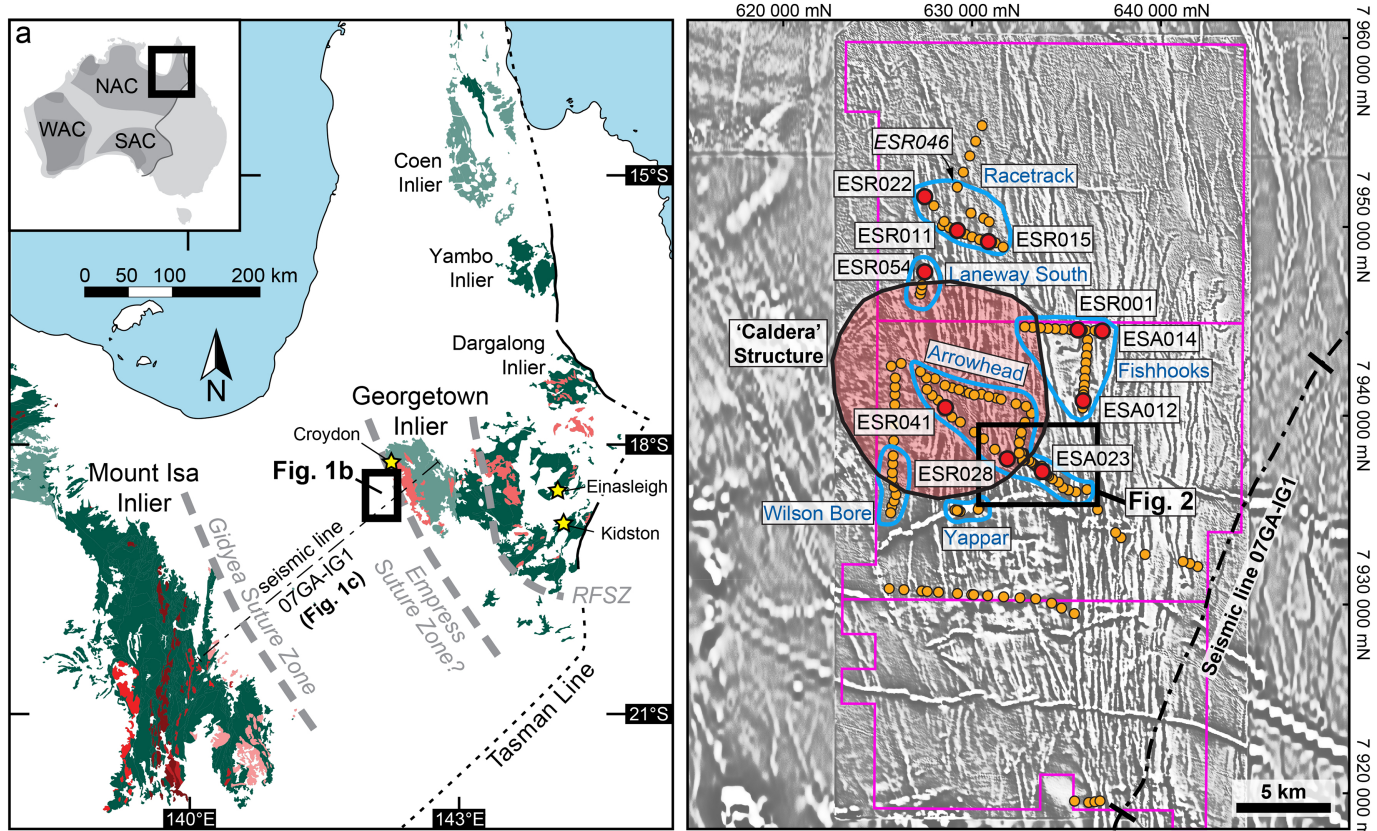
*Olierook et al.,
Table 1*

Graphical abstract

Highlights

- Granite emplacement, mafic–felsic volcanism and mafic intrusions occurred at 1560–1550 Ma at the Au-Ag-Zn-Pb Empress Springs Project.
- Plagioclase alteration to sericite at ca. 330–250 Ma, possibly coeval with mineralization
- Ag/Au ratio ~ 1 , mineral associations and age of mineralization points to epithermal system
- Refined position of suture zone between North Australian Craton and Laurentia proposed, termed the Empress Springs Suture Zone

Journal Pre-proof



Sedimentary successions

- light green: lower Mesoproterozoic
- dark green: upper Paleoproterozoic

Intrusive rocks

- red: 1.50 Ga (top) to 1.85 Ga (bottom)

- red circle: Dated drill holes
- orange circle: Other drill holes
- blue circle: Prospects
- pink outline: 2019 Empress Springs tenement boundary

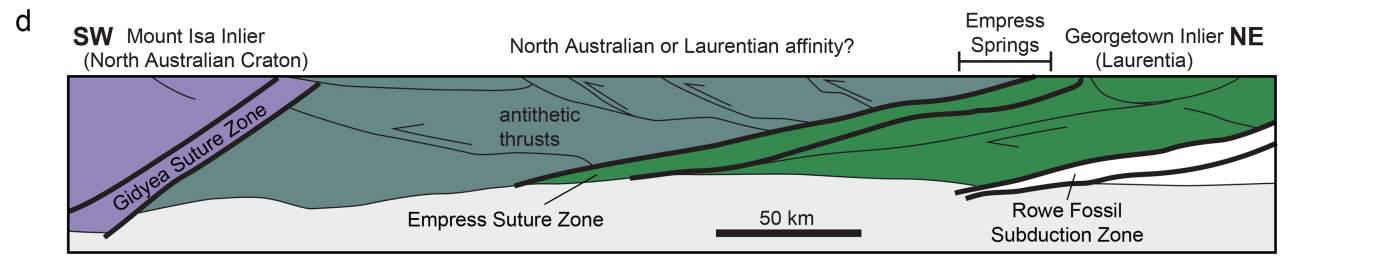
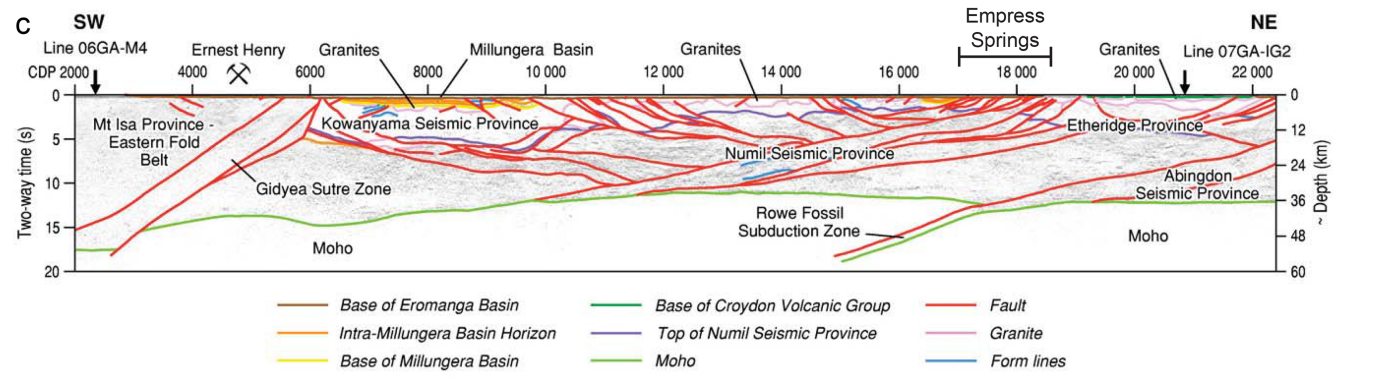
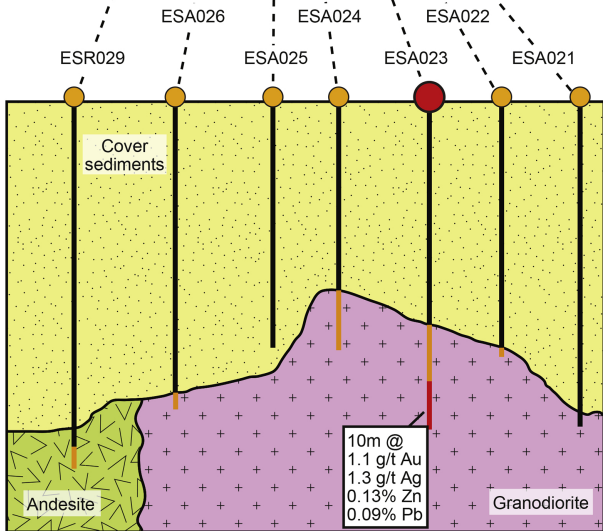
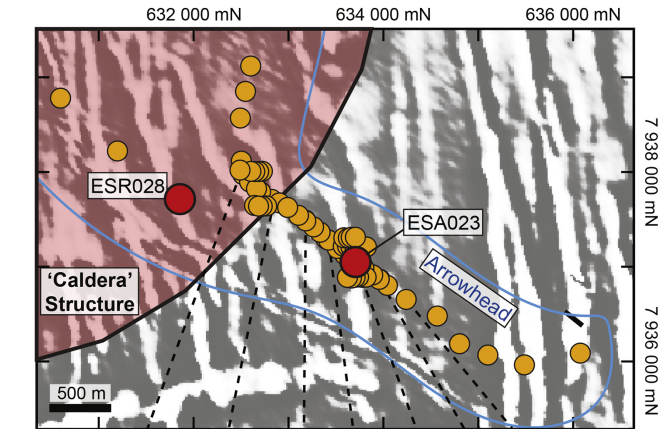


Figure 1



Cu (ppm)	9	31	41	100	3
Pb (ppm)	57	19	250	960	15
Zn (ppm)	120	120	450	1610	100

Figure 2

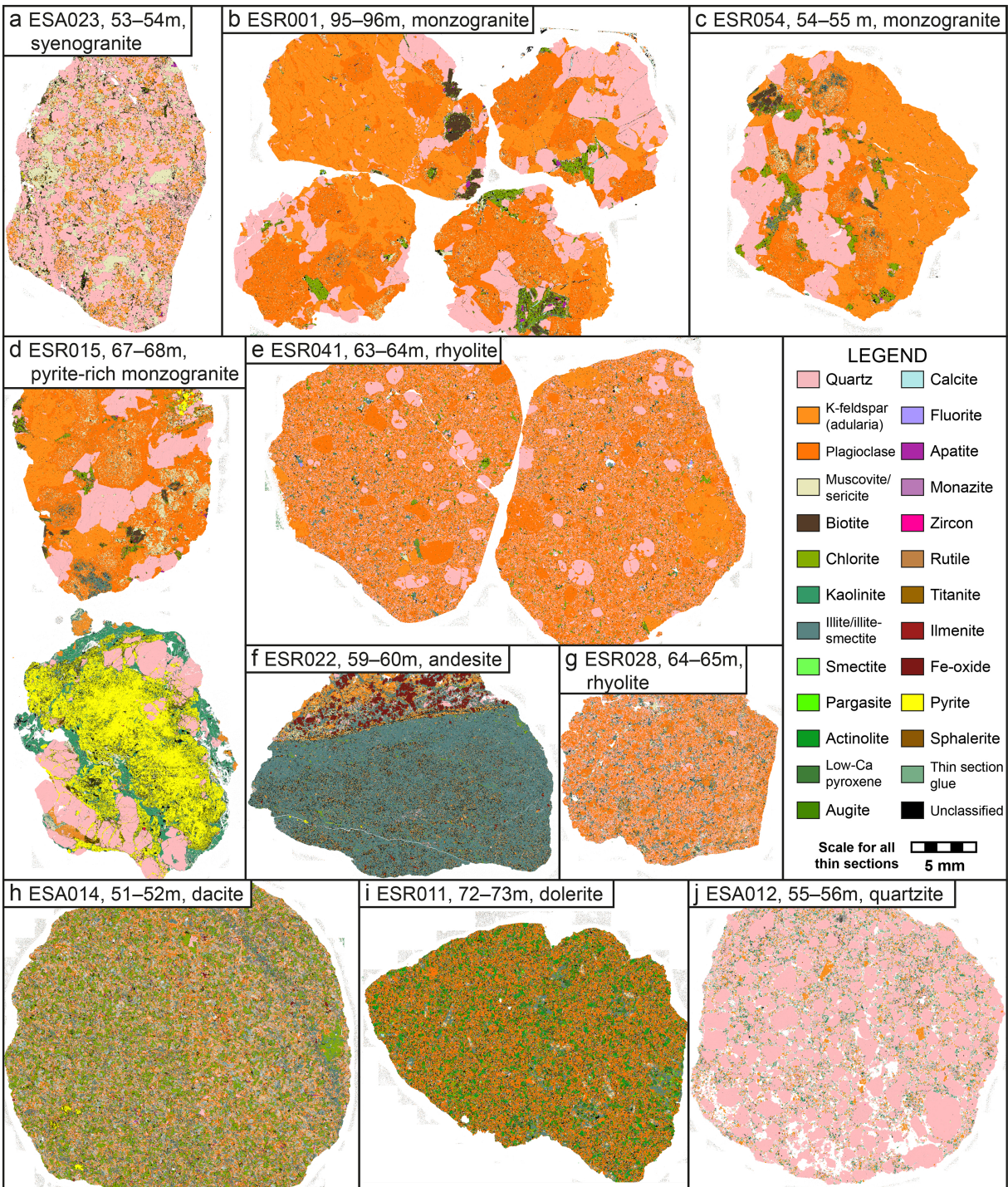
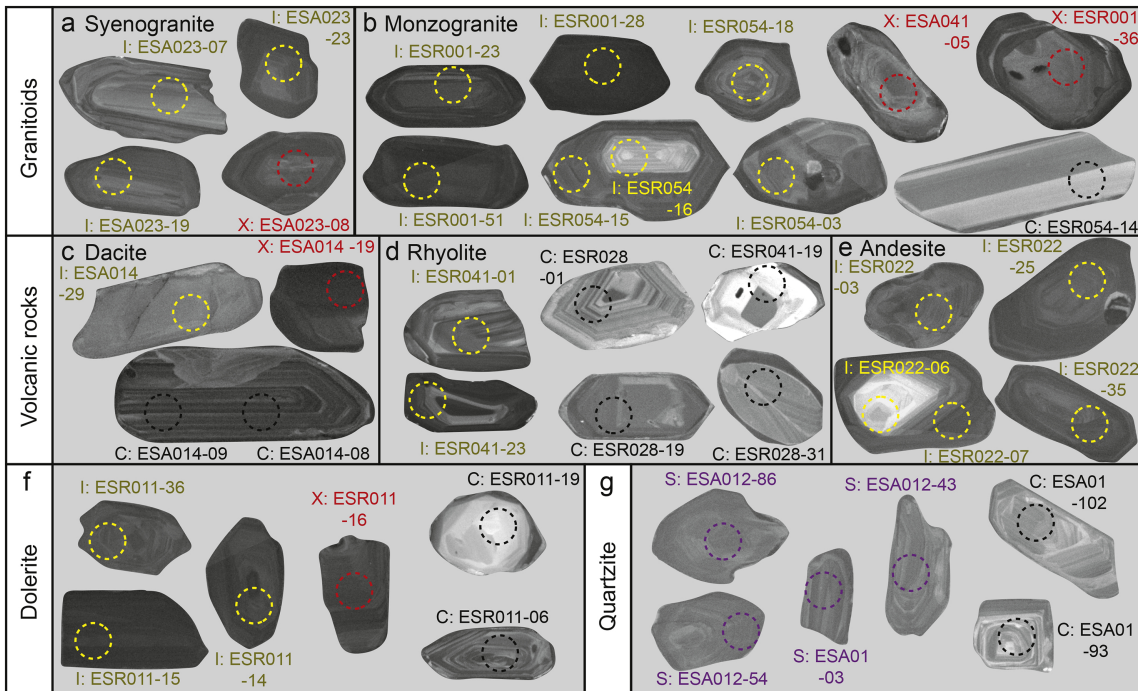


Figure 3




Scale for all
 CL images  100 μm

Figure 4

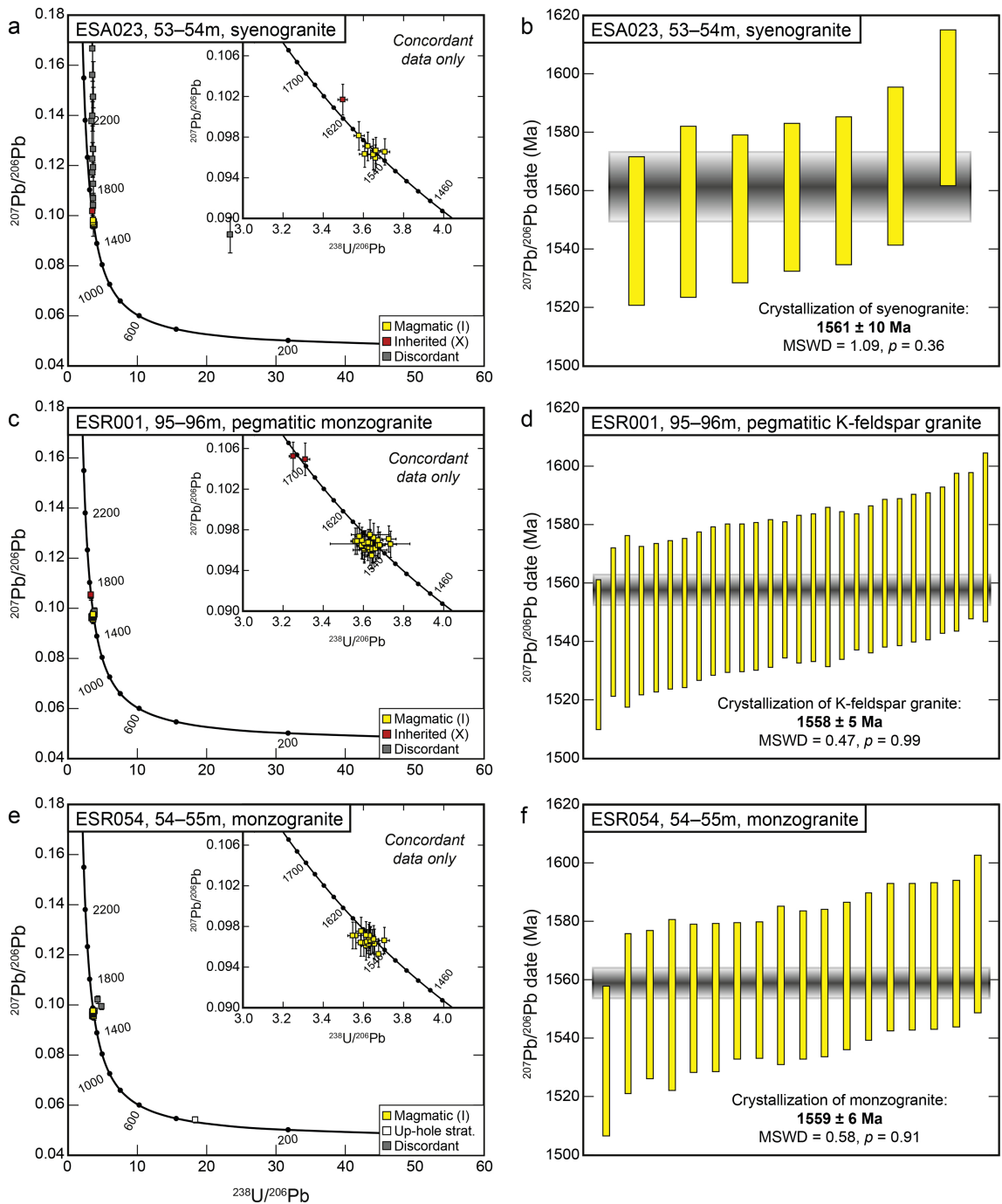


Figure 5A

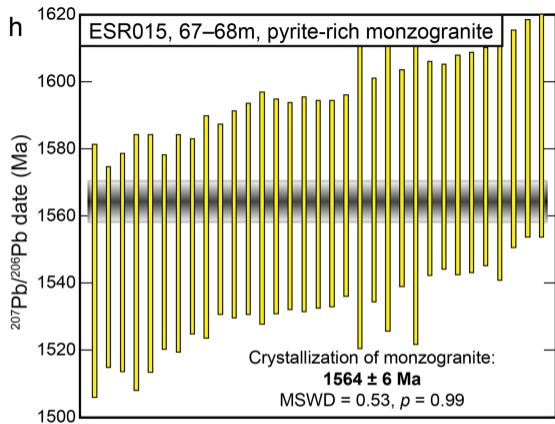
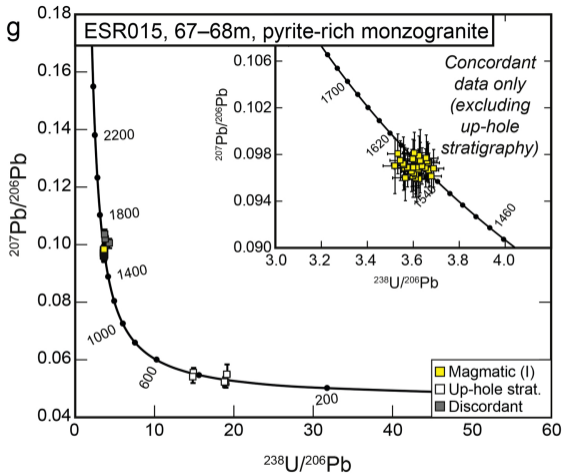


Figure 5B

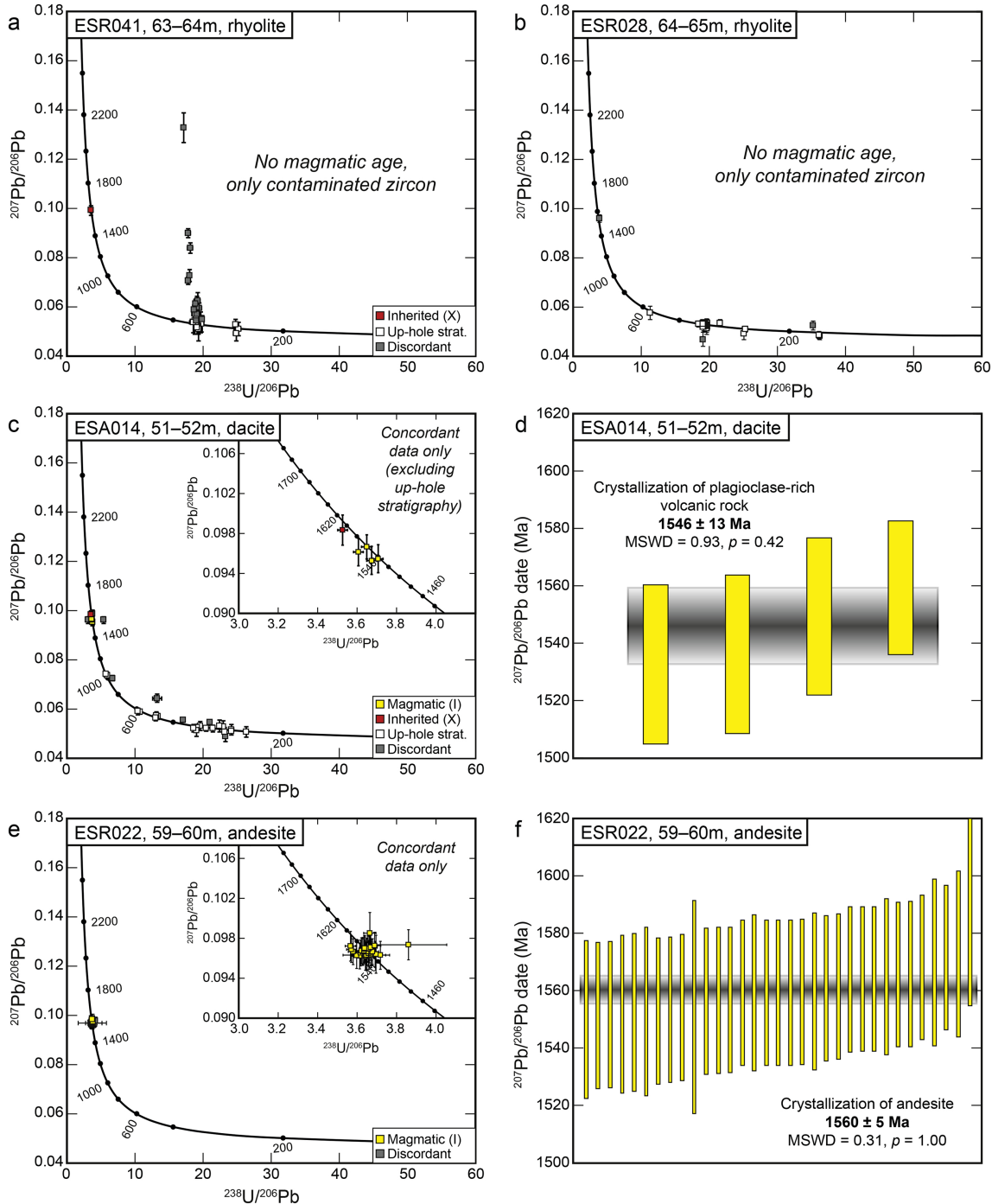


Figure 6

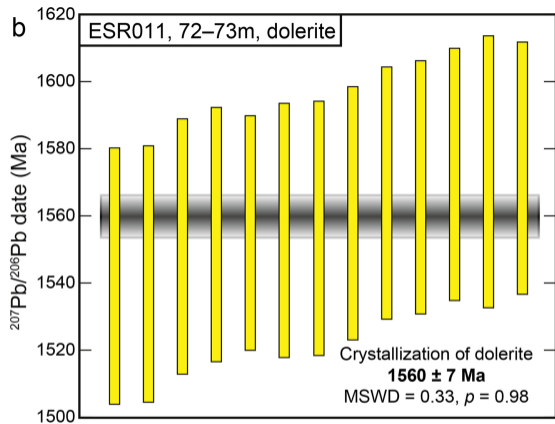
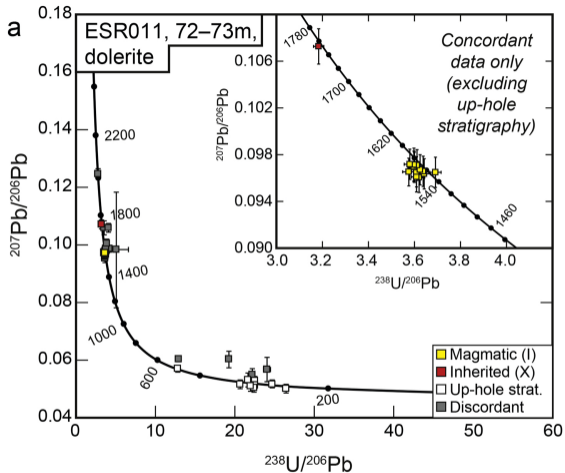


Figure 7

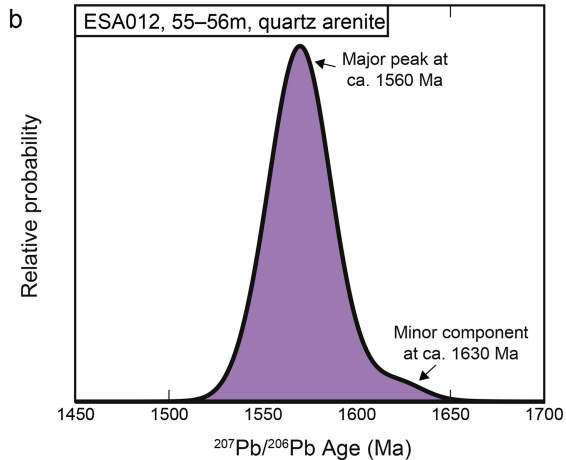
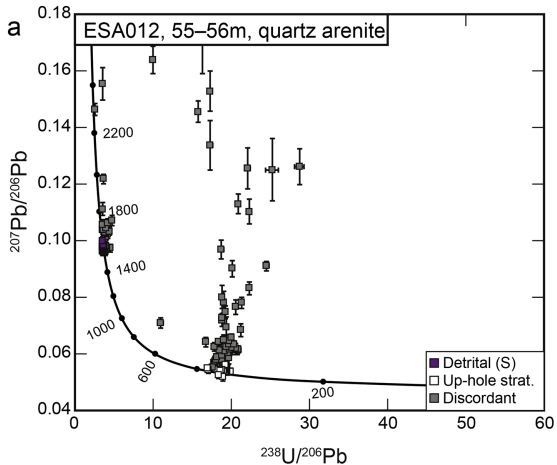


Figure 8

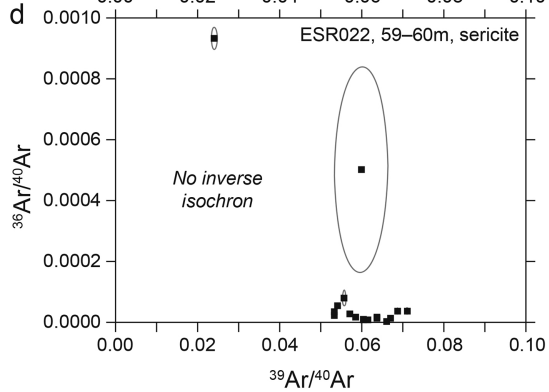
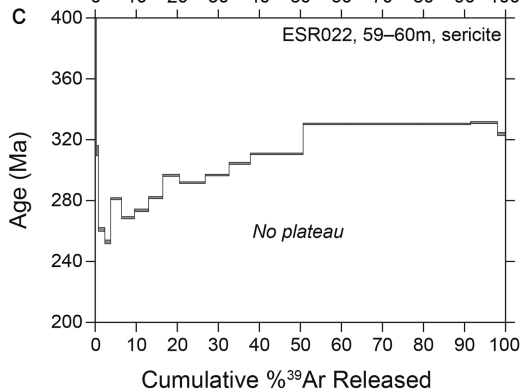
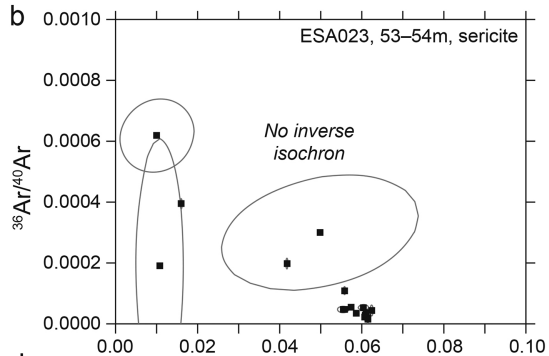
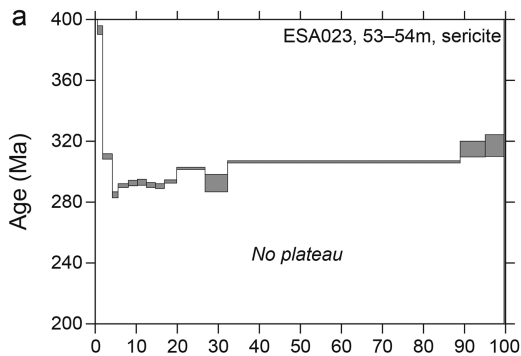


Figure 9

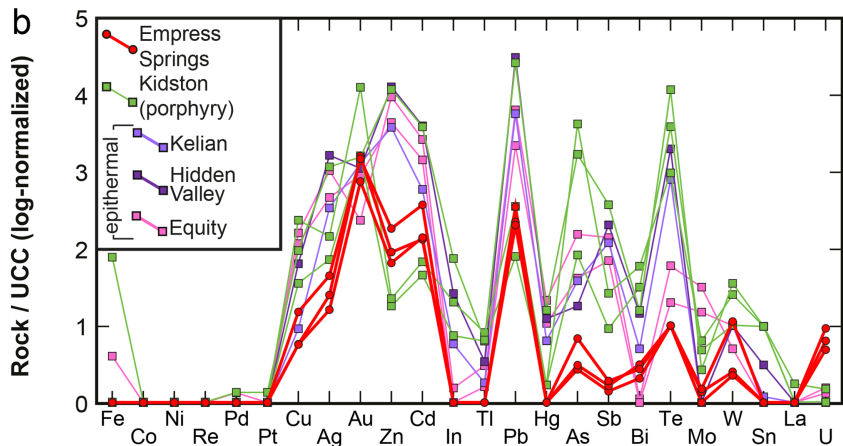
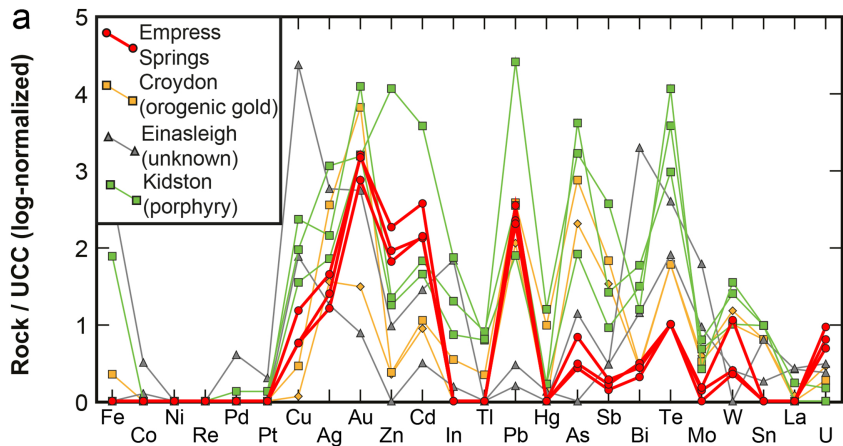


Figure 10

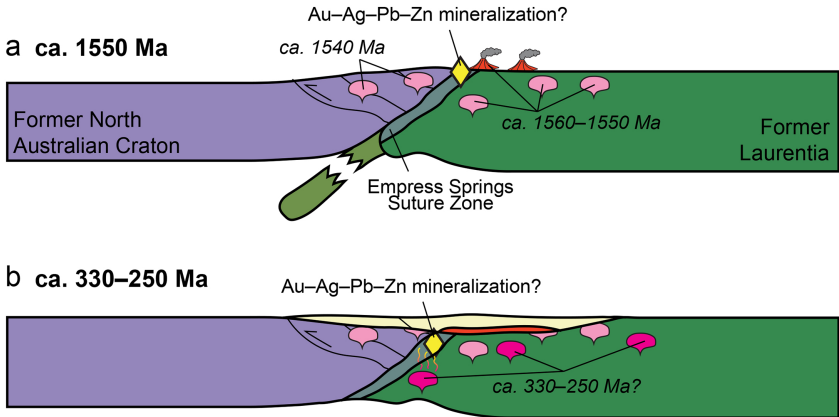


Figure 11